On elastic anisotropy of 3D printed acrylonitrile butadiene styrene structures

Ashraf Kasmi, Joseph Marae Djouda, François Hild

On Elastic Anisotropy of 3D printed Acrylonitrile Butadiene Styrene Structures

Ashraf Kasmi[a,b], Joseph Marae Djouda[a,c*], François Hild[a]

[a]Université Paris-Saclay, CentraleSupélec, ENS Paris-Saclay, CNRS, LMPS-Laboratoire de Mécanique Paris-Saclay, 4 avenue des Sciences, 91190 Gif-sur-Yvette, France

[b]Université PSL, ENS Paris-Ulm, 45 rue d'Ulm, 75005 Paris, France

[c]ERMESS, EPF-Engineering School, 3 bis Rue Lakanal, 92330 Sceaux, France

Abstract

Material extrusion is one of the most widespread additive manufacturing processes because of its low-cost implementation and its flexibility in design. In this study, integrated digital image correlation is used for the identification of constitutive parameters of two configurations of acrylonitrile butadiene styrene (ABS) samples. It is shown that an isotropic elastoplastic model calibrated from *one* single edge notched tension specimen described correctly the behavior of 3D printed ABS parts independently of the internal infill strategy.

Keywords: Acrylonitrile butadiene styrene, Elastic anisotropy, Integrated digital image correlation, Material extrusion, Single edge notched specimen

Corresponding author:
Joseph MARAE DJOUDA

List of variables and abbreviations

α	Tikhonov parameter
β	Hardening coefficient
$\{\delta \boldsymbol{p}\}$	Material parameter vector increment
$\{\boldsymbol{\varepsilon}\}$	Strain vector (with components ϵ_{ij})
$\{\boldsymbol{\varepsilon^e}\}$	Elastic strain vector
$\{\boldsymbol{\varepsilon^p}\}$	Plastic strain vector
γ_i	Standard deviation of acquisition noise
γ_u	Standard displacement uncertainty
γ_F	Standard force uncertainty
ν	Poisson's ratio
χ_i^2	Image cost function
χ_{iF}^2	Total cost function
χ_F^2	Force cost function
$\boldsymbol{\sigma}$	Stress tensor
$\{\boldsymbol{\sigma}\}$	Stress vector (with components σ_{ij})
σ_{eq}	Von Mises equivalent stress
σ_U	Ultimate tensile strength
σ_y	Yield stress
$\boldsymbol{\sigma}^D$	Stress deviator tensor
ϕ	Yield function
$\boldsymbol{\psi_k}$	Shape functions
a_c	Computed nodal displacement
a_k	Unknown nodal displacement
$\{\boldsymbol{b}\}$	DIC residual vector
$\{\boldsymbol{b_i}\}$	Image residual vector
$\{\boldsymbol{b_{iF}}\}$	Total residual vector
$\{\boldsymbol{b_F}\}$	Force residual vector
$\left[\boldsymbol{C_p}\right]$	Parameter covariance matrix
$[\boldsymbol{D}]$	Stiffness matrix (with components D_{ij}) in the specimen reference frame
E	Young's modulus
$f(\boldsymbol{x})$	Gray level of reference image
F_c	Computed force
F_m	Measured force
$g(\boldsymbol{x}+\boldsymbol{u}(\boldsymbol{x}),t)$	Gray level of deformed pictures corrected by measured displacement field
$[\boldsymbol{H_i}]$	Image Hessian matrix
$[\boldsymbol{H_{iF}}]$	Total Hessian matrix
$[\boldsymbol{H_F}]$	Force Hessian matrix
$\boldsymbol{I}$	Second order identity tensor
$[\boldsymbol{M}]$	DIC matrix
N_i	Number of pixels in the ROI
N_t	Number of time-steps
p	Cumulated plastic strain
$\{\boldsymbol{p}\}, \{\boldsymbol{p}_0\}$	Material parameter vector, and initial values
$[\boldsymbol{Q}]$	Stiffness matrix (with components Q_{ij}) in the layer reference frame
R	Isotropic hardening variable

$\{\boldsymbol{S_F}\}$	Force sensitivity vector
$[\boldsymbol{S_u}]$	Displacement sensitivity matrix
t	Time-step
$[\boldsymbol{T_{strain}}(\theta_j)]$	Rotation matrix associated with angle θ_j
$[\boldsymbol{T_{stress}}(\theta_j)]$	Rotation matrix associated with angle θ_j
$\boldsymbol{u}(\boldsymbol{x})$	Displacement field
w_j	Thickness fraction of layer
$\boldsymbol{x}$	Position vector
ABS	Acrylonitrile butadiene styrene
AM	Additive manufacturing
DIC	Digital image correlation
FDM	Fused deposition modeling
FEMU	Finite element model updating
FEMU-F	Finite element model updating with force data
FFF	Fused filament fabrication
I-DIC	Integrated digital image correlation
NOD	Notch opening displacement
PLA	Polylactic acid plastic
ROI	Region of interest
Q4	Four-noded quadrilaterals
SENT	Edge notched tensile test

1. Introduction

The use of additive manufacturing (AM) techniques in material fabrication has become very popular in the last decade [1,2]. This trend occurred in several industrial domains and impacts the way of designing structures, which is due to the flexibility of design and fabrication, in particular for materials with complex geometries [1]. AM also has the advantage of reducing production time, of low cost production and is environment friendly [3-6]. AM is composed of various techniques that are related to the material to be used. Among them, material extrusion also called "fused filament Fabrication" (FFF) or "Fused Deposition Modeling" (FDM), is widespread for the fabrication of polymer structures [6]. Material extrusion has been mainly developed for thermoplastic materials such as Acrylonitrile Butadiene Styrene (ABS) and Polylactic Acid plastic (PLA).

In order to bring AM to the level of traditional fabrication routes, the relationship between the fabrication parameters (e.g., deposited layer thickness, deposition speed, temperature, layer angle and orientation), the mechanical properties and their changes during in-service life have to be fully understood [7]. The variation of fabrication parameters during the process significantly affects the material properties [8,9]. It would be tedious and expensive to solely study experimentally this relationship between process, material and properties. Rivet et al. [10] used dimensional analyses to establish the relationship between raw and 3D-printed materials in order to reduce by two thirds the number of required characterization configurations. The numerical identification of material parameters is then relevant for limiting the number of experimental case studies.

The effect of build parameters on anisotropy properties of parts obtained by material extrusion have been characterized [11–13]. The influence of raster orientation, bead width, air gap and temperature during the fabrication process on the tensile strength has been demonstrated. The bead orientation and printing density appear as parameters that influence anisotropy of parts obtained by material extrusion. Using a free design code (G-code), Koch et al. [14] showed that a control of bead orientation, layer height and printing density improved the mechanical properties of the obtained parts in comparison to injection molding. The printing artifacts relative to infill challenges at the part edge may affect the mechanical properties (and their anisotropy) during loading as well. It is then necessary to investigate such anisotropy in order to accurately design AM parts. The existing empirical models are not suited for such descriptions [15,16] because they are not based on constitutive laws. Xia et al. [15] proposed an anisotropic model combined with Hill plasticity. This model was based on the combination

of mechanical parameters obtained from specimens printed in five different orientations (0°, 30°, 45°, 60° and 90°).

The identification of material parameters has been widely developed [11-14]. The utilization of full field measurements in conjunction with inverse problem solution is widespread. Two of the main routes are the Virtual Fields Method [15-17] and Finite Element Model Updating (FEMU) [11,13,18-20]. Another method that bypasses the previous two-step strategies, namely, full field measurement and subsequent identification is Integrated Digital Image Correlation (or I-DIC) [20-24] in which the identification procedure starts from images and provides direct access to material parameters. In appropriate conditions, weighted FEMU and I-DIC yield results which are very close [19] and optimal [31] in terms of uncertainties. In I-DIC, the gap between the experiment and simulations in terms of gray level residuals and applied forces is minimized simultaneously.

In the present study, I-DIC was used for the identification of mechanical parameters of additively manufactured ABS with a *single* Edge Notched Tensile Test (SENT) specimen. The filaments were deposited following two different patterns, namely, (i) a classical ± 45° lay-up, and (ii) a so-called oriented deposition [32]. The I-DIC identification scheme has not yet been implemented for such type of material, despite the effort made for the characterization of ABS parts obtained by material extrusion [33]. In the present analyses, the need to account for elastic anisotropy was investigated. Conversely, in the elastoplastic regime, only isotropic hardening was considered. Images acquired at two different scales allowed the calibrated parameters to be probed globally or locally close to the notch root. In the following, the experimental and numerical methods will be detailed. Concerning the experimental configuration, the specimen fabrication and the tensile tests are presented. In the numerical methods, the constitutive framework is defined as well as the I-DIC framework. Then, the results of the parameter calibration for the two sample configurations are presented and discussed in terms of elastic anisotropy.

2. Experimental and numerical methods

2.1. Specimen preparation

The specimens used herein were obtained by material extrusion with dimensions shown in Figure 1(a). During fabrication, the ABS filament was heated at 235°C and deposited through a nozzle layer by layer. The thickness of the deposited layer and of the walls, which ensured the good shape of the specimen, was 0.25 mm and 0.3 mm, respectively. The MakerBot replicator

2X was used to print samples with two orientations, namely, a classical ± 45° layup (Figure 1(b)), and an oriented deposition (Figure 1(c)). In this last configuration, the layers were deposited in order to follow the principal stress directions in the specimen for the region close to the notch root. For the other part of the sample, the filaments were oriented 0° (along tensile direction). It was shown that the mechanical properties were enhanced mainly in terms of fracture toughness for this configuration [34]. The notch in the specimens was also 3D printed. The thickness of the fabricated samples was initially 6 mm in order to avoid any surface effect (roughness), the two sides were then mechanically polished in order to reach a thickness of 3 mm, and to make the speckle deposition easier for digital image correlation purposes [35].

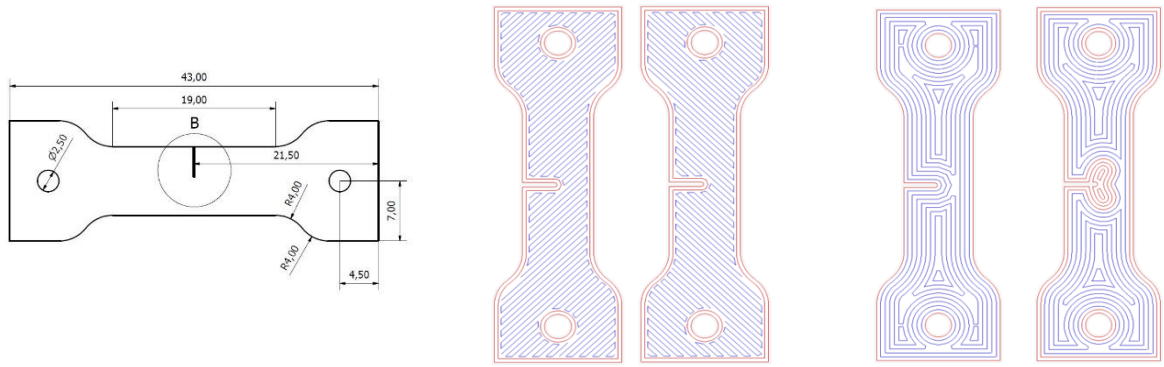

(a) (b) (c)

Figure 1 - (a) Dimensions (in mm) of SENT samples fabricated via material extrusion modeling. Infill of specimen with ± 45° (b) and oriented (c) depositions.

After the printing process, because of temperature effects and dimensions of the notch, the latter was initially closed. For the ± 45° specimen, a 200-µm thick blade was used to reopen the notch. Last, before each mechanical test, speckles were sprayed onto each specimen surface in accordance to the resolution of the visualization system, which was used for image acquisitions.

2.2. Tensile tests

Figure 2Figure 2(a) shows the experimental set-up that allowed for multiscale characterizations. It was constituted by one camera with a telecentric lens in order to monitor the whole sample surface (Figure 2(b)), which corresponds to the macroscopic scale. In addition, a Keyence VHX 1000 microscope was used to obtain information at the mesoscale from the other specimen surface (Figure 2(c)). During in-situ tensile tests, the samples were continuously loaded with an INSTRON 5982 testing machine, in which a 9 kN load cell was mounted in series. The applied stroke speed was 3.5 µm/s, and one frame per second was acquired with both optical systems.

The acquisition and classification of images and loading data were managed by the trigger of the testing machine.

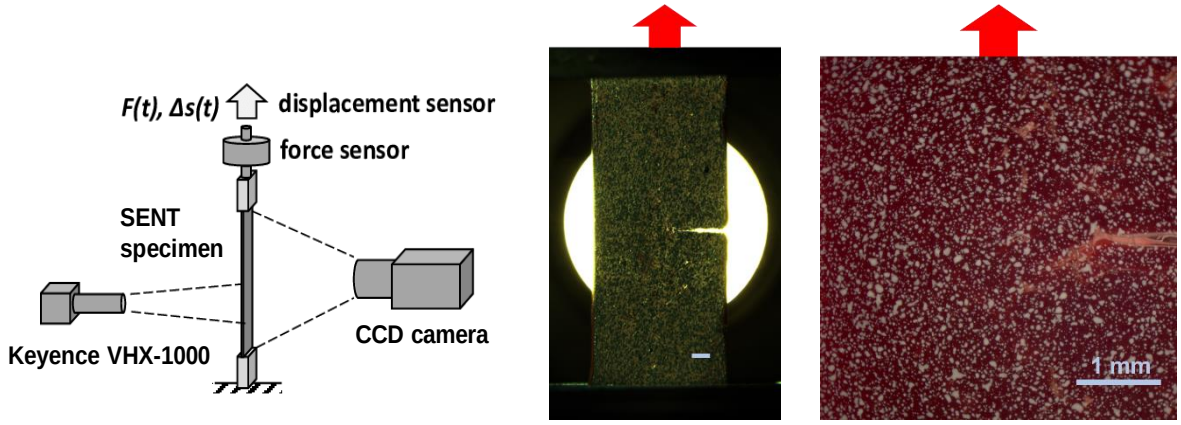

(a) (b) (c)

Figure 2 - (a) Schematic drawing of the experimental setup. (b) Macroscopic image acquired with the telecentric length, and (c) corresponding mesoscopic obtained with the Keyence VHX 1000. The red arrows indicate the tensile direction and the scale have the same value: 1 mm.

Considering the force-displacement plots of both tests (Figure 3), it is observed that the force reached a maximum level before decreasing and final failure. By the time the sample reached this point, a crack had initiated from the notch root and then propagated (observed on the acquired images) thus plateauing the force level. Crack initiation was the consequence of damage near the notch root, and led to a sharp decrease of the force level in the ± 45° sample because of sudden breakage of weld lines between filaments. In the optimized sample, the trajectory of the filaments during deposition allows it to better resist against crack propagation [34–36]. However, because of infill challenges, the porosity content is higher in the material bulk and thus may lower its ultimate tensile strength. The ± 45° sample that contains less defects in the material bulk has a higher ultimate tensile strength.

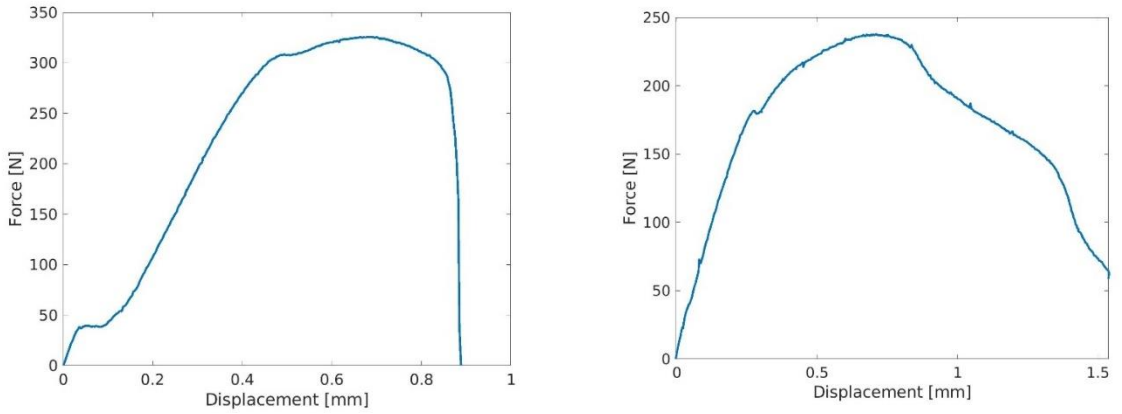

(a) (b)

Figure 3 - Force-displacement plots of (a) ± 45° (b) optimized SENT samples. A higher maximum force is observed in the ± 45° case, and larger maximum displacement in the optimized configuration.

Once the experiment was conducted, images and load measurements were acquired, and the net-section stress-strain response was subsequently plotted. Since the samples were notched, net section stresses (NSS) were evaluated to compute the macroscopic response of the material (Figure 4). The NSS is the ratio of the applied force during the test by the initial ligament surface. The global strain was obtained from the displacement of the grips of the micromachine. The NSS – strain curves thus correspond to the macroscopic response of such samples.

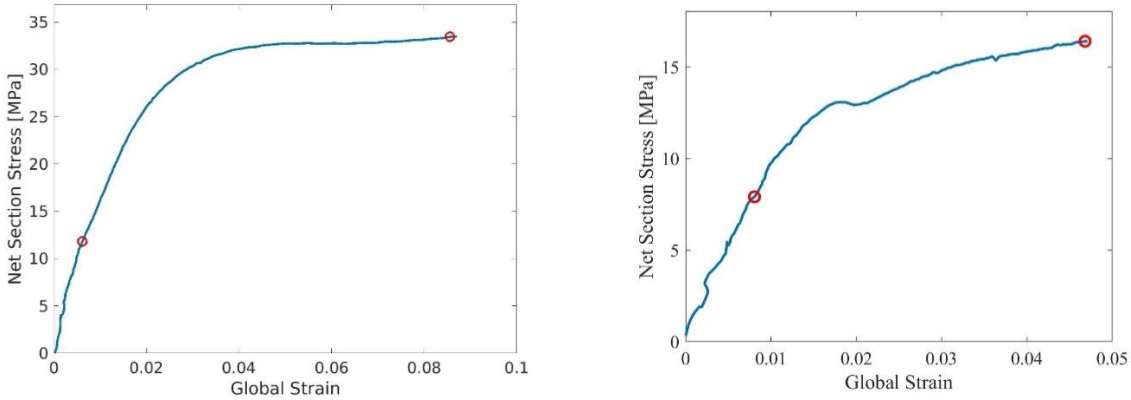

(a) (b)

Figure 4 - Net section stress-strain plots for the ± 45° (a) and optimized (b) SENT specimens. The red circles depict the end of elastic and elastoplastic phases.

The red circles, indicating the end of the elastic and elastoplastic phases, were determined by considering the grey level residual images and following crack propagation. The identification was divided into two parts. First, the elastic regime of the experiment in which both isotropic-elastic and orthotropic-elastic models were probed. Second, for the elastoplastic regime, isotropic-elastic/isotropic-plastic and orthotropic-elastic/isotropic-plastic models were investigated.

2.3. Digital image correlation

The acquired images were processed via Digital Image Correlation (DIC), which is an experimental technique that measures displacement fields [37]. DIC consists in registering a series of pictures of the sample before and during the deformation process, and returning displacement fields and gray level residuals. The FE-based approach consists in selecting a region of interest (ROI) on the reference image, and meshing it using finite elements (e.g., with four-nodded Q4 quadrilaterals [38] or three-nodded triangles (T3) [39]). Then, the displacement field is estimated at the nodes of each element for each time-step. The same mesh may also be used in numerical simulations to calibrate material parameters [19,37]. Note that kinematic data (i.e., displacement fields) only provide dimensionless quantities such as Poisson's ratio or the ratio of yield stress to Young's modulus, and that the identification of other dimensional parameters requires additional measurements such as the applied forces at each time-step [19].

DIC relies on the minimization of a cost function that contains information from the images with respect to the sought displacement field. In the present case, the cost function is the sum of squared differences between the gray levels of the reference image f and the deformed pictures g corrected by the sought displacement field $\boldsymbol{u}(\boldsymbol{x})$ [19]

$$\chi_i^2(\boldsymbol{u}(\boldsymbol{x}),t) = \frac{1}{2\gamma_i^2 N_i}\sum_{ROI}\big(g(\boldsymbol{x}+\boldsymbol{u}(\boldsymbol{x}),t) - f(\boldsymbol{x})\big)^2 \quad (1)$$

where $\boldsymbol{x}$ is the pixel position, t the time-step, and N_I the number of pixels in the region of interest (ROI). The factor 2 before the variance γ_i^2 comes from the fact that noise exists in both reference and deformed images. The displacement field is decomposed as

$$\boldsymbol{u}(\boldsymbol{x}) = \sum_k a_k \boldsymbol{\psi_k}(\boldsymbol{x}) \quad (2)$$

where $\boldsymbol{\psi_k}$ are shape functions, and a_k the unknown kinematic degrees of freedom (here nodal displacements). The sought displacement field is then found using a Gauss-Newton iterative scheme in order to minimize χ_i^2 with respect to all unknowns a_k. Successive linearizations of the summand in the cost function are applied, and then corrections to the nodal displacement are iteratively updated [37].

2.4. Identification method

2.4.1. Constitutive Laws

The total strain tensor is divided into elastic and plastic parts (using Voigt notation)

$$\{\boldsymbol{\varepsilon}\} = \{\boldsymbol{\varepsilon^e}\} + \{\boldsymbol{\varepsilon^p}\} \quad (3)$$

where $\{\boldsymbol{\varepsilon}\}$ denotes the column vector gathering all strain components. In the elastic-isotropic model, the stress vector is given by

$$\begin{Bmatrix}\sigma_{11}\\ \sigma_{22}\\ \sigma_{33}\\ \sigma_{12}\\ \sigma_{13}\\ \sigma_{23}\end{Bmatrix} = \frac{E}{(1+\nu)(1-2\nu)}\begin{bmatrix}1-\nu & \nu & \nu & & & \\ \nu & 1-\nu & \nu & & 0 & \\ \nu & \nu & 1-\nu & & & \\ & & & (1-2\nu)/2 & & \\ & 0 & & & (1-2\nu)/2 & \\ & & & & & (1-2\nu)/2\end{bmatrix}\begin{Bmatrix}\varepsilon_{11}^e\\ \varepsilon_{22}^e\\ \varepsilon_{33}^e\\ \gamma_{12}^e\\ \gamma_{13}^e\\ \gamma_{23}^e\end{Bmatrix} \quad (4)$$

where E is Young's modulus and ν Poisson's ratio. In the elastic-orthotropic model, the stress vector is given by (in the reference frame of the considered layer)

$$\begin{Bmatrix}\sigma_{11}\\ \sigma_{22}\\ \sigma_{33}\\ \sigma_{12}\\ \sigma_{13}\\ \sigma_{23}\end{Bmatrix}_{local} = \begin{bmatrix}Q_{11} & Q_{12} & Q_{13} & & & \\ Q_{12} & Q_{22} & Q_{23} & & 0 & \\ Q_{13} & Q_{23} & Q_{33} & & & \\ & & & Q_{44} & & \\ & 0 & & & Q_{55} & \\ & & & & & Q_{66}\end{bmatrix}\begin{Bmatrix}\varepsilon_{11}^e\\ \varepsilon_{22}^e\\ \varepsilon_{33}^e\\ \gamma_{12}^e\\ \gamma_{13}^e\\ \gamma_{23}^e\end{Bmatrix}_{local} \quad (5)$$

whereas the stress vector in the specimen frame is expressed as

$$\begin{Bmatrix}\sigma_{11}\\ \sigma_{22}\\ \sigma_{33}\\ \sigma_{12}\\ \sigma_{13}\\ \sigma_{23}\end{Bmatrix}_{global} = \begin{bmatrix}D_{1111} & D_{1122} & D_{1133} & & & \\ D_{1122} & D_{2222} & D_{2233} & & 0 & \\ D_{1133} & D_{2233} & D_{3333} & & & \\ & & & D_{1212} & & \\ & 0 & & & D_{1313} & \\ & & & & & D_{2323}\end{bmatrix}\begin{Bmatrix}\varepsilon_{11}^e\\ \varepsilon_{22}^e\\ \varepsilon_{33}^e\\ \gamma_{12}^e\\ \gamma_{13}^e\\ \gamma_{23}^e\end{Bmatrix}_{global} \quad (6)$$

In order to determine whether plasticity is activated, one may use Von Mises criterion to define the yield function ϕ

$$\phi = \sigma_{eq} - \sigma_y - R(p) \quad (7)$$

with σ_y the yield stress, R the isotropic hardening variable (dependent on the cumulated plastic strain p), and σ_{eq} the Von Mises equivalent stress

$$\sigma_{eq} = \sqrt{\frac{3}{2}\boldsymbol{\sigma}^D : \boldsymbol{\sigma}^D} \quad \text{with} \quad \boldsymbol{\sigma}^{\boldsymbol{D}} = \boldsymbol{\sigma} - \frac{tr(\boldsymbol{\sigma})}{3}\boldsymbol{I} \quad (8)$$

where σ is the stress tensor, σ^D its deviatoric part, $tr(.)$ the trace of a second order tensor, and $\boldsymbol{I}$ the second order identity tensor. In the present case, Voce's hardening law [40] was selected

$$R(p) = \left(\sigma_U - \sigma_y\right)\left(1 - e^{-\beta p}\right) \quad (9)$$

where σ_U is the ultimate tensile strength, and β the hardening coefficient.

Since the samples were made of several layers with different orientations, the global material parameters of the sample

$$\{\boldsymbol{\sigma_{global}}\} = [\boldsymbol{D}]\,\{\boldsymbol{\varepsilon^{e}_{global}}\} \tag{10}$$

are estimated using the local properties of each layer

$$\{\boldsymbol{\sigma_{local}}\} = [\boldsymbol{Q}]\,\{\boldsymbol{\varepsilon^{e}_{local}}\} \tag{11}$$

and one needs to calculate the stiffness tensor of each layer in the sample frame, and then sum (considering the thicknesses of different layers) the stiffness tensors of different layers after rotation

$$[\boldsymbol{D}] = \sum_{j,layers} w_j \left[\boldsymbol{T_{stress}}(\theta_j)\right]\,[\boldsymbol{Q}]\,\left[\boldsymbol{T_{strain}}(\theta_j)\right]^{-1} \tag{12}$$

where w_j is the thickness fraction of layer j, $[\boldsymbol{D}]$ the stiffness tensor using global coordinates, $[\boldsymbol{Q}]$ the stiffness tensor using local coordinates, and $\boldsymbol{T_{stress}}(\theta_j)$ the rotation tensor with an angle θ_j. This computation is only performed in the elastic-orthotropic case (with possibly 6 parameters to be identified). Even though the layers had a transversely isotropic behavior, the sample may exhibit an anisotropic behavior because of different layer orientations. For the sake of simplicity, the plastic behavior was assumed to be isotropic and modeled using Voce's law (with 3 parameters to be identified) for any choice of elastic description.

2.4.2. Integrated DIC

Integrated DIC was used to identify the sought material parameters gathered in the column vector $\{\boldsymbol{p}\}$. The inputs (big) data were the images acquired during the experiment, and the output (key) data were the optimized parameters $\{\boldsymbol{p}\}$. I-DIC relies on the minimization of the sum of squared differences between both the reference image $f(\boldsymbol{x})$ *and* the measured forces F_m on the one hand, and the corrected deformed images by the computed displacement field $g(\boldsymbol{x} + \boldsymbol{u_c}(\boldsymbol{x}, t, \{\boldsymbol{p}\}))$ and the computed resultant forces $F_c(\{\boldsymbol{p}\}, t)$ with respect to the set of material parameters. Displacement residuals (i.e., differences between DIC displacement fields and computed ones), force residuals (differences between measured and computed forces) and sensitivity fields (how the displacement field and load measurement change with the material parameters) are also returned at the end of this process. The Dirichlet boundary conditions used in the simulations were extracted from the experiment using DIC at each time-step [19]. The I-

DIC process was implemented within the Correli 3.0 framework (written in MATLAB and C++) [41].

The image-force cost function of I-DIC is written with respect to the sought parameters $\{\boldsymbol{p}\}$ [19]

$$\chi_{iF}^2(\{\boldsymbol{p}\}) = \frac{1}{2}\chi_i^2(\{\boldsymbol{p}\}) + \frac{1}{2}\chi_F^2(\{\boldsymbol{p}\}) \tag{13}$$

with χ_i^2 the image cost function

$$\chi_i^2(\{\boldsymbol{p}\}) = \frac{1}{2\gamma_i^2 N_i N_t}\sum_t \sum_{ROI}\Big(g\big(\boldsymbol{x} + \boldsymbol{u_c}(\boldsymbol{x}, t, \{\boldsymbol{p}\})\big) - f(\boldsymbol{x})\Big)^2 \tag{14}$$

and χ_F^2 the force cost function

$$\chi_F^2(\{\boldsymbol{p}\}) = \frac{1}{\gamma_F^2 N_t}\sum_t\big(F_m(t) - F_c(t, \{\boldsymbol{p}\})\big)^2 \tag{15}$$

where N_i is the number of pixels in the ROI, N_t the number of time-steps, F_m the measured force, $\boldsymbol{u_c}$ the computed displacement field, and F_c the computed force. The summation over time indicates that the sought material parameters should be valid for all time-steps [26].

The optimized set of parameters $\{\boldsymbol{p}\}$ is found using a Gauss-Newton iterative scheme in which successive linearizations are applied, and successive corrections $\{\delta\boldsymbol{p}\}$ to the set of material parameters are estimated [27]

$$\{\delta\boldsymbol{p}\} = [\boldsymbol{H_{iF}}]^{-1}\{\boldsymbol{b_{iF}}\} \tag{16}$$

where the total Hessian and residual vector read

$$[\boldsymbol{H_{iF}}] = \frac{1}{2}[\boldsymbol{H_i}] + \frac{1}{2}[\boldsymbol{H_F}] \tag{17}$$

$$\{\boldsymbol{b_{iF}}\} = \frac{1}{2}\{\boldsymbol{b_i}\} + \frac{1}{2}\{\boldsymbol{b_F}\} \tag{18}$$

with

$$[\boldsymbol{H_i}] = \frac{1}{2\gamma_i^2 N_i N_t}\sum_t[\boldsymbol{S_u}(\boldsymbol{x}, t)]^T\,[\boldsymbol{M}]\,[\boldsymbol{S_u}(\boldsymbol{x}, t)] \tag{19}$$

$$\{\boldsymbol{b_i}\} = \frac{1}{2\gamma_i^2 N_i N_t}\sum_t[\boldsymbol{S_u}(\boldsymbol{x}, t)]^T\,\{\boldsymbol{b}\} \tag{20}$$

$$[\boldsymbol{H_F}] = \frac{1}{\gamma_F^2 N_t}\sum_t\{\boldsymbol{S_F}(t)\}\,\{\boldsymbol{S_F}(t)\}^T \tag{21}$$

$$\{\boldsymbol{b_F}\} = \frac{1}{\gamma_F^2 N_t}\sum_t \{\boldsymbol{S_F}(t)\}\left(F_m - \widetilde{F_c}\right) \tag{22}$$

as well as the nodal displacement $[\boldsymbol{S_u}]$ and force $\{\boldsymbol{S_F}\}$ sensitivity matrices

$$[\boldsymbol{S_u}(\boldsymbol{x}, t)] = \left[\frac{\partial \boldsymbol{a_c}}{\partial\{\boldsymbol{p}\}}\right] \tag{23}$$

$$\{\boldsymbol{S_F}(t)\} = \left\{\frac{\partial F_c}{\partial\{\boldsymbol{p}\}}\right\} \tag{24}$$

and the computed nodal displacement a_c and force F_c, measured force F_m, DIC matrix $[\boldsymbol{M}]$ and DIC residual vector $\{\boldsymbol{b}\}$

$$M_{ij} = \sum_{ROI}\left(\boldsymbol{\psi_i}(\boldsymbol{x}) \cdot \boldsymbol{\nabla_x} f(\boldsymbol{x})\right)\left(\boldsymbol{\psi_j}(\boldsymbol{x}) \cdot \boldsymbol{\nabla_x} f(\boldsymbol{x})\right) \tag{25}$$

$$b_i = \sum_{ROI}\left(f(\boldsymbol{x}) - g\left(\boldsymbol{x} + \tilde{\boldsymbol{u}}(\boldsymbol{x})\right)\right)\left(\boldsymbol{\psi_i}(\boldsymbol{x}) \cdot \boldsymbol{\nabla_x} f(\boldsymbol{x})\right) \tag{26}$$

In order to evaluate the sensitivity matrices, the displacement field is computed through multiple simulations in which one parameter is changed at a time, and then the elements of the sensitivity matrices are calculated through a finite differences scheme [26]. For example, a first simulation is run using the current set of parameters to obtain the reference values of $a_c^{(j)}$ and $F_c^{(j)}$. Then N_p simulations are performed in which one parameter is increased 1% at a time, with N_p being the number of parameters.

The total Hessian matrix is an indicator of identifiability and is related to the parameter covariance matrix by

$$\left[\boldsymbol{C_p}\right] = [\boldsymbol{H_{iF}}]^{-1}\left(\frac{1}{2N_i N_t}[\boldsymbol{H_i}] + \frac{1}{2N_t}[\boldsymbol{H_F}]\right)[\boldsymbol{H_{iF}}]^{-1} \tag{27}$$

Each eigenvalue of the Hessian corresponds to an eigenvector (or eigen parameter) constructed as a linear combination of material parameters. The lower the eigenvalues of the covariance matrix (i.e., the higher the eigenvalues of the Hessian), the more reliable the identification of its eigenvector. For instance, the covariance matrix indicates how to optimize a mechanical test when investigating a certain parameter set, particularly, by modifying the shape and geometry of the sample [26].

The problem to solve herein was 2D with plane stress elements (CPS3), the shear strains γ_{13} and γ_{23} were vanishing, as well as $\sigma_{13} = \sigma_{23} = \sigma_{33} = 0$. Since Q_{66} only appears in the expressions of D_{1313} and D_{2323}, it was not activated (Equation (6)). This insensitivity makes

the inversion of the image-force Hessian impossible because of zero sensitivity related to Q_{66} in the Hessian matrix. Hence, a Tikhonov regularization was implemented, which consists in penalizing variations with respect to the initial set of parameters $\{\boldsymbol{p}_0\}$

$$[\boldsymbol{H_{tot}}] = [\boldsymbol{H_{iF}}] + \alpha[\boldsymbol{I}] \tag{28}$$

$$\{\boldsymbol{b_{tot}}\} = \{\boldsymbol{b_{iF}}\} + \alpha\left\{\frac{\widetilde{\boldsymbol{p}}-\boldsymbol{p}_0}{\boldsymbol{p}_0}\right\} \tag{29}$$

where α is the Tikhonov parameter. Thus, the unidentifiable eigen parameters whose eigenvalue is less than the Tikhonov parameter will not evolve (or very slightly) during the minimization process. Prescribing a too low Tikhonov parameter will cause oscillations in the sought parameters, which hinder convergence. One needs to search for the lowest possible Tikhonov parameter without causing such oscillations. The Tikhonov parameter for the present analyses was found to be equal to 3×10^{-3} multiplied by the highest eigenvalue of the Hessian matrix $[\boldsymbol{H_{iF}}]$.

2.4.3. Sensitivity Analysis

The force sensitivity matrix provides a scalar per parameter for each time-step (Figure 5) whereas the nodal *x*-*y*-displacements provide two sensitivity *fields* per parameter for each time-step. An estimation of the temporal displacement sensitivity is obtained by evaluating the standard deviation of all node displacements at each time-step (for *x* and *y* directions, thus two scalars, one for each component) and then the corresponding root mean square yields one scalar per time-step (Figure 5).

The curves corresponding to the parameter Q_{66} have a zero value all along the experiment, which was expected. The sensitivities of the plastic parameters, notably the ultimate stress σ_U, increase at the end of the experiment, since plasticity is getting more and more activated. This effect is also associated with a decrease of the force-sensitivities of the elastic parameters since more and more elements are yielding. However, the displacement sensitivity of the hardening coefficient β increases as well but its level remains limited. The corresponding force sensitivity is almost equal to zero along the experiment. The elastic parameters Q_{13} and Q_{44} have high displacement sensitivities in the end of the experiment, and high force sensitivity in the middle of the experiment.

Conversely, Q_{11} and Q_{22} have good sensitivities, especially for displacements, which constantly increase along the experiment whereas the force sensitivities increase, then start to decrease near image 150 because of the activation of plasticity in more and more elements in

the mesh. The parameter Q_{23} has the same tendencies, yet with lower values. Thus, one expects that parameters Q_{11}, Q_{22} and σ_y have the highest identifiability given their sensitivities, and that it will be more difficult to extract the hardening coefficient β in comparison to the other parameters.

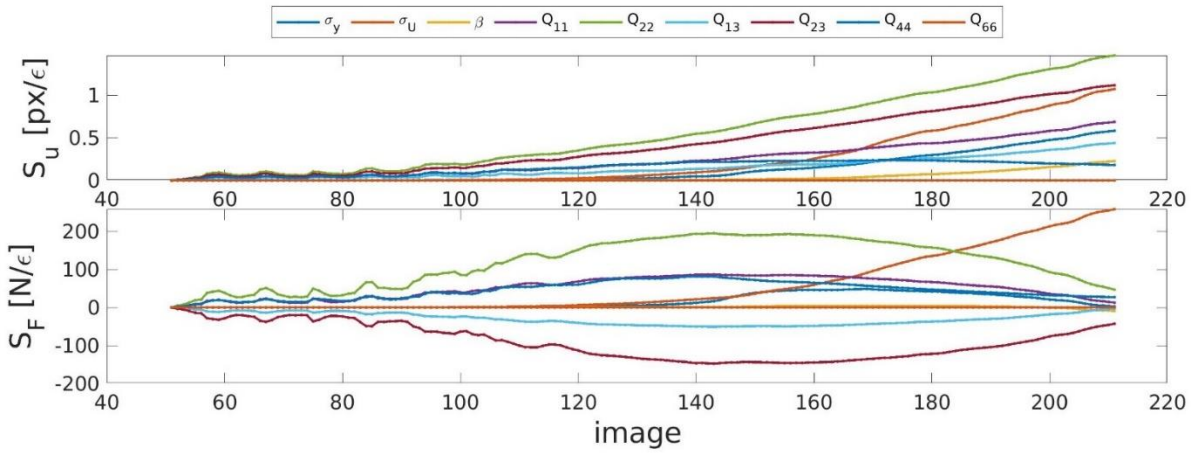

Figure 5 - Global displacement [px/perturbation factor] and force [N/perturbation factor] sensitivities as functions of image number for all elastoplastic parameters using an orthotropic elastoplastic model.

2.4.4. First Estimation of Identifiability

Once the sensitivity matrices are calculated, they are used to evaluate the different dimensionless Hessians (image, force and image-force, see Equations (17), (19) and (21)). They are diagonalized to determine the eigen values and the corresponding eigen parameters (Figure 6). If an eigenvalue is much higher than one, then the eigen parameter is deemed identifiable. This observation means that judging whether a parameter is identifiable requires looking at the eigen parameters rather than each individual parameter alone.

In Figure 6, from the eigenvectors of the image-force Hessian, the ultimate strength σ_U is mainly represented by the first and second eigen parameters (second line of the image-force eigenvectors matrix) whose eigenvalues are much larger than one (~10^5 and ~10^3). Hence, the ultimate strength σ_U is identifiable. Conversely, the elastic parameter Q_{66} is only represented by the ninth eigenvector, which has zero eigenvalue since it was not activated during the tensile experiment. This parameter is not identifiable, and its value will never evolve during the identification process (thanks to the Tikhonov regularization). Moreover, the hardening coefficient β is mainly represented by the sixth eigenvector, which has a modest eigenvalue of nearly 1, which makes its identifiability questionable. This weak identifiability comes from its aforementioned small displacement and force sensitivities.

It is worth noting that the total sensitivity comes from both image *and* force Hessians, and that some parameters have larger or smaller image-sensitivities than force sensitivities. For example, the elastic parameter Q_{44} is mainly represented by the third eigenvector of the image-Hessian, which has an eigenvalue of nearly 1 (questionable identifiability). Conversely, the parameter Q_{44} is mainly represented by the fourth eigenvector of the force-Hessian, which has an eigenvalue of about 10^2 (good identifiability). Thus, Q_{44} is identifiable using the total image-force Hessian. In that case, the force Hessian is dominant. These observations suggest that one should launch several identifications using different initializations in order to check which parameters tend to evolve or tend to remain close to their initial value, thus giving a complementary idea on their identifiability. This point is also used to make sure that the converged solution was not trapped in some local minimum (which is one of the major risks of such ill-posed problems).

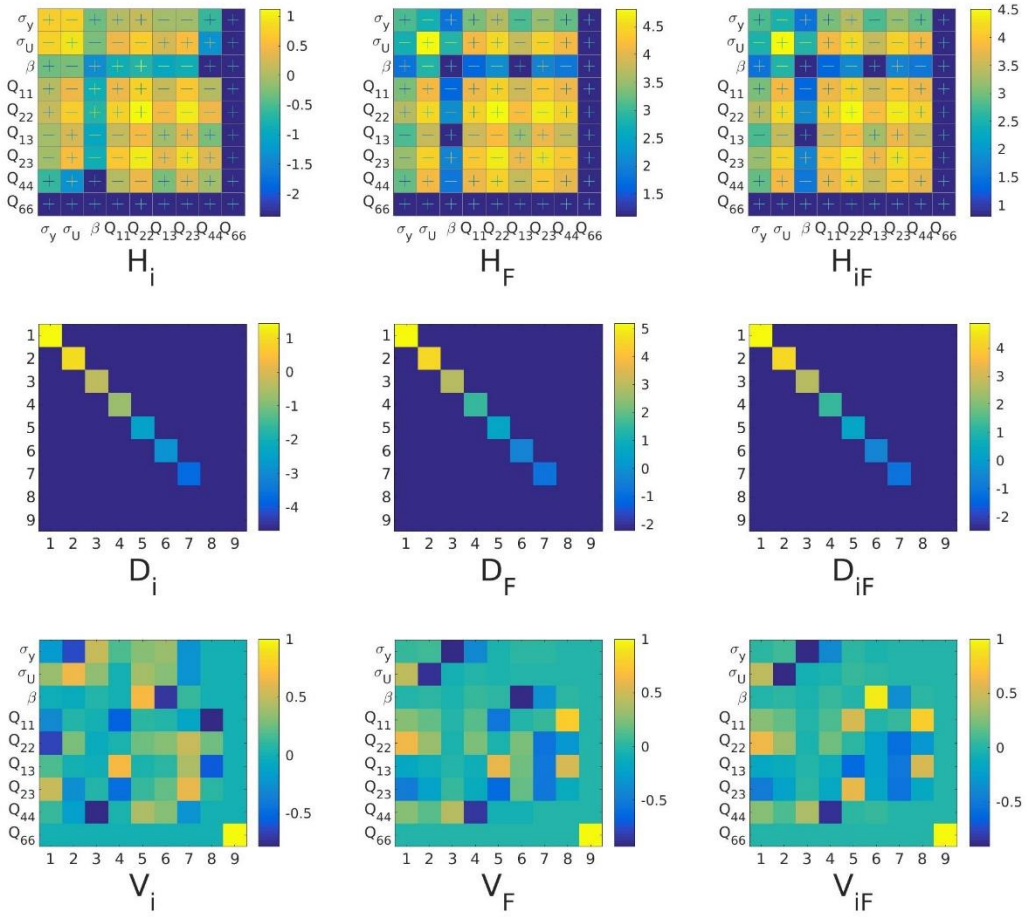

Figure 6 - Absolute image (left column), force (middle column) and image-force (right column) Hessians of the initial estimation (log_{10} scale, first row), with their eigenvalues (log_{10} scale, second row) and the corresponding eigenvectors (third row).

3. Identification Results

3.1. ± 45° orientation

3.1.1. Uncertainty Quantification

One important step before launching the identification process is to estimate the various uncertainties, namely, standard deviations of gray levels, displacement, and load measurements. The preliminary phase of the experiment was exploited when no load was applied (images 0-50). For acquisition noise, the temporal standard deviation of each pixel was calculated throughout the preliminary phase, and then, a root mean squared estimation was assessed for all pixels in order to obtain a single scalar for the entire ROI. For the displacement field, the temporal standard deviation of each nodal displacement was calculated and plotted (Figure 7) in which it is noted that the horizontal component of the standard displacement uncertainty is globally smaller than the vertical one. Further, the standard displacement uncertainty is lower in the center than near the contours since the elements near the latter suffer from the absence of information outside the mesh. A mean squared estimation was assessed for all nodes in order to obtain a single scalar for each displacement component. Last, a mean squared estimation was computed for both *x* and *y*-components to obtain a unique scalar reported in Table 1.

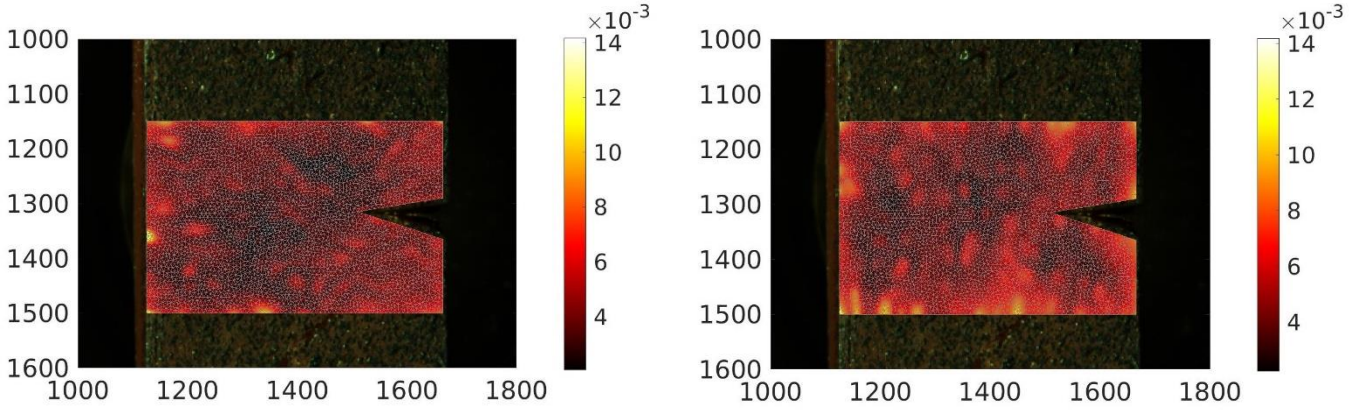

Figure 7 - Horizontal (a) and vertical (b) components of the standard displacement uncertainty fields [px], element length = 5px.

For the load measurements, the standard deviation was also calculated in the preliminary phase (Figure 8(a)). The end of this preliminary phase was determined using the notch opening displacement (NOD), which represents the displacement difference between two nodes on each side of the notch (Figure 8(b)). Before load application, the NOD had a vanishingly small value (Figure 8(b)), and once the load was applied the *x*-component of the NOD fluctuated around

zero (i.e., mode I dominant loading) whereas the *y*-component started to increase indicating the beginning of the notch opening.

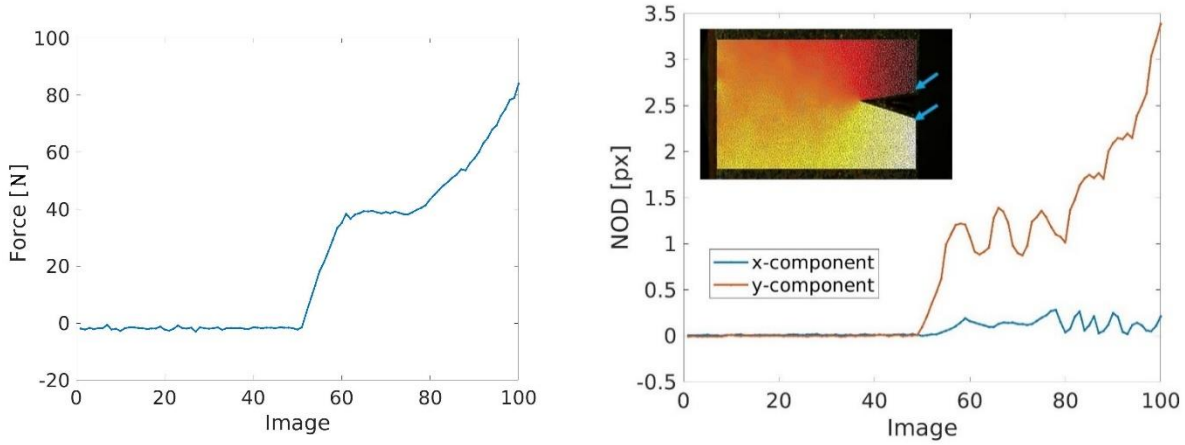

(a) (b)

Figure 8 - (a) Force as a function of image number illustrating measurement fluctuations before image 51, and load application thereafter (beginning of the experiment).
(b) NOD as a function of image number also illustrating the beginning of the experiment at image 51.

Table 1 summarizes the standard uncertainties that were later used to compute the various dimensionless residuals. Note that the relatively low values of the uncertainties indicate that the experimental conditions were good, which is very interesting to probe the various models selected herein.

Table 1 - Standard uncertainties of acquisition noise, displacement, and force

$\gamma_i\ [GL]$	$\gamma_u\ [px]$	$\gamma_F\ [N]$
1.1	$4.5\ 10^{-3}$	0.44

3.1.2. Identification and code convergence

After calculating the image-force Hessian, the image-force residual vector was calculated and the Tikhonov regularization was applied in order to obtain the total Hessian and residual vector. The total (regularized) Hessian was then inverted and the parameter corrections were found (Equation (16)). The process of residual evaluation was repeated at the end of each iteration in order to track their changes, and follow the minimization of total residual (Figure 9(a)). If the convergence criterion was fulfilled (correction per iteration of each parameter less than 0.5%), the identification was stopped. Otherwise, a new iteration was started. Note that the maximum correction per iteration of each parameter was set to 10%. It is noteworthy that I-DIC needs the

material parameters to be initialized. In the isotropic case, the Poisson's ratio was set to 0.3 whereas the Young's modulus was initialized using a classical fit on the stress-strain plot (Figure 3). In the orthotropic case, the parameters were initialized using the isotropic parameters.

After convergence, the total residual was lowered by a factor of 4 (Figure 9(a)) indicating that the solution corresponds to a minimum (in the present case, it is believed to be a global one since several sets of initial parameters were tested). Figure 9(b) shows how the parameter corrections decreased and tended to zero, thereby indicating the fulfillment of the convergence criterion. The change of dimensionless parameters (divided by their initial values) is shown in Figure 9(c). The ultimate tensile strength σ_U was the parameter that evolved the most (Figure 9(b-c)). This trend comes from the fact that a fine mesh was used, which allowed a clearer description of the strain gradients near the notch root (Figure 13Figure 10), and hence, provided a more accurate description of yielding.

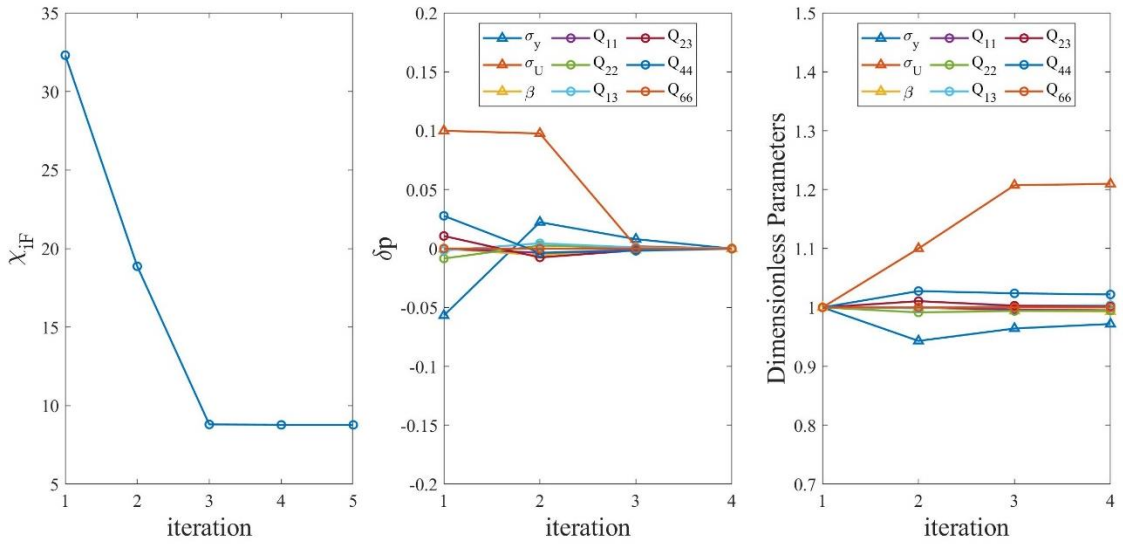

(a) (b) (c)

Figure 9 - Change of total residuals (a), corrections on dimensionless parameters (b), and change in dimensionless parameters (c) as functions of iteration number showing the convergence of I-DIC using an orthotropic elastoplastic model.

The minimization of the total residual does not correspond to the individual minimization of image and force residuals (Figure 10). In the present case, the image residual increased a bit (from 4.63 to 4.69), whereas the force decreased very significantly (from 45 to 12) and much more than the increase in image residual (≈ 0.06). The displacement residual, which was not minimized, increased by ≈ 3.8 and followed the same trend as the image residual. These two residuals are correlated as they account for kinematic aspects either evaluated at the

pixel scale (for integrated DIC) or at the nodal scale (when comparing measured via FE-based DIC and computed displacement fields).

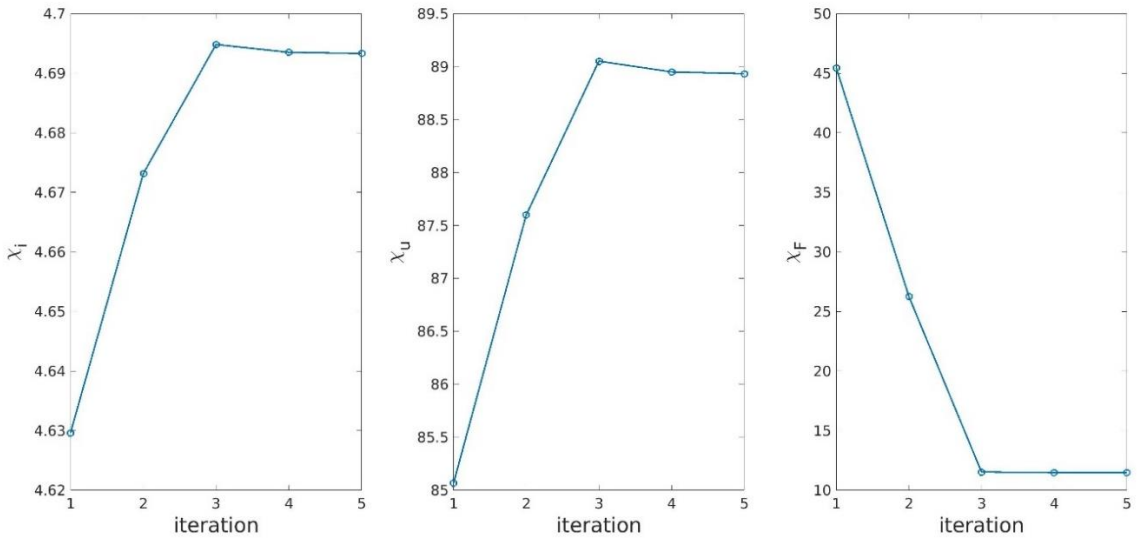

(a) (b) (c)

Figure 10 - Change of image (a), displacement (b) and force (c) residuals as functions of iteration number.

The different instantaneous residuals as functions of image number are reported in Figure 11. Two regimes are observed, notably on the image and force data (Figure 11(a-b)): a first elastic regime (images 51-111), and then an elastoplastic one (images 111-211). During the elastic phase, the image residual for DIC and I-DIC (Figure 11(a)) nearly coincided, thereby indicating that the hypothesis of elasticity was satisfied (i.e., no model error). The force residual (Figure 11(b)) fluctuated, and had higher levels compared to those in the elastoplastic phase since the boundary conditions prescribed in simulations were measured (i.e., via DIC); the signal to noise ratio was lower in the elastic regime than in the elastoplastic phase. Moreover, the displacement residuals also kept low values during this first phase thanks to the good description of elasticity (Figure 11(c-d)).

During the elastoplastic phase, a small gap between the image residuals of DIC and I-DIC is seen, and increased further because of crack initiation and the associated damage mechanism that were not modeled. This trend is also associated with drastic increases in displacement residuals since damage was not considered (as seen previously, the displacement residuals followed the same tendency as image residuals). The rapid increase in displacement residuals with the applied load is thus associated with damage development. The force residual,

however, remained fairly low in the elastoplastic phase, which indicates that the main features were captured by the calibrated model (Figure 11).

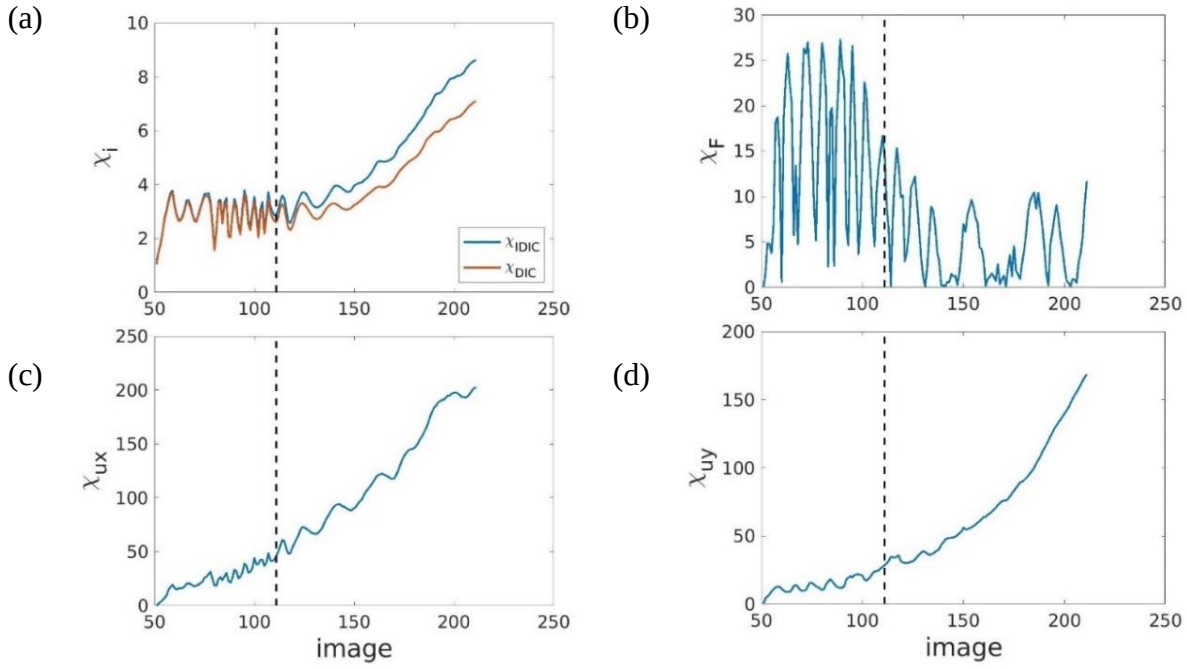

Figure 11 - Instantaneous image (a), force (b) and displacement (c-d) residuals as functions of image number. The dashed vertical lines depict the end of the elastic regime and the transition to the elastoplastic regime.

3.1.3. Calibrated parameters

The results of the elastic analysis (using images 51-111) were used to estimate the residuals on elastic (images 51-111), elastoplastic (images 51-211, by extrapolation) and damage (images 51-251, by extrapolation) regimes (see Table 2). The same computations were also conducted using the results of the elastoplastic analysis (using images 51-211). In the elastic domain (images 51-111), the residuals were very close for *all* models (a difference of 1 is not considered a major improvement). However, the orthotropic elastoplastic model had 9 degrees of freedom whereas the orthotropic elastic model had 6, the isotropic elastoplastic model had 5, and the isotropic elastic model had only 2 degrees of freedom. Hence, it was expected that when the number of degrees of freedom in the model was increased, the residual would decrease, but the computation time would increase.

From the results of Table 2, it is concluded that an *isotropic* elastic model is a very good compromise in this regime. In the elastoplastic domain (images 51-211), the residuals using elastic models were extremely high compared to those using elastoplastic laws. A model error occurred since the material underwent yielding. Comparing again isotropic and orthotropic models suggests that the difference was negligible compared to the needed computation time,

namely, the orthotropic model took roughly twice the time assuming isotropic elasticity. The result with the isotropic elastoplastic model using I-DIC is deemed optimal since it represents a very good compromise between a low total residual ($\chi_{tot} = 9.3$) and a low computation time. This result was not expected from the literature review [32,42] since additively manufactured materials were assumed to suffer from strong elastic anisotropy.

The FEMU-F method was also used (i.e., only the force functional was minimized, and images were not considered), and gave good results, namely, the image-force residual was of the same order of magnitude as I-DIC and since no images were processed, the code ran much faster than I-DIC. FEMU-F can thus be used in order to obtain a very good initialization of the material parameters.

Table 2 - Residuals using different constitutive models and image sets, element length = 5px. The bold cells indicate that the residual was computed for calibration ranges

Regime	Elastic (images 51-111)		Elastoplastic (images 51-211)		
Model	Isotropic I-DIC	Orthotropic I-DIC	Isotropic I-DIC	Orthotropic I-DIC	Orthotropic FEMU-F
χ_{iF} (Images 51-111)	**13.1**	**11.9**	13	12.2	16.9
χ_{iF} (Images 51-211)	222	206	**9.3**	**8.8**	**11.5**
χ_{iF} (Images 51-251)	542	508	30	27	38

Using the sensitivity matrices obtained at convergence of I-DIC, the different Hessians (image, force and total) were evaluated and are shown in Figure 12. They were diagonalized and can be used as in the aforementioned manner. The new identifiabilities are in line with the *a priori* predictions of Figure 5, namely, the ultimate tensile strength σ_U still had a very high sensitivity followed by the parameter Q_{22}, then the yield stress σ_y and Q_{44}. Conversely, the parameters Q_{11}, Q_{13} and Q_{23} achieved modest identifiability, and Q_{66} still had zero identifiability as expected.

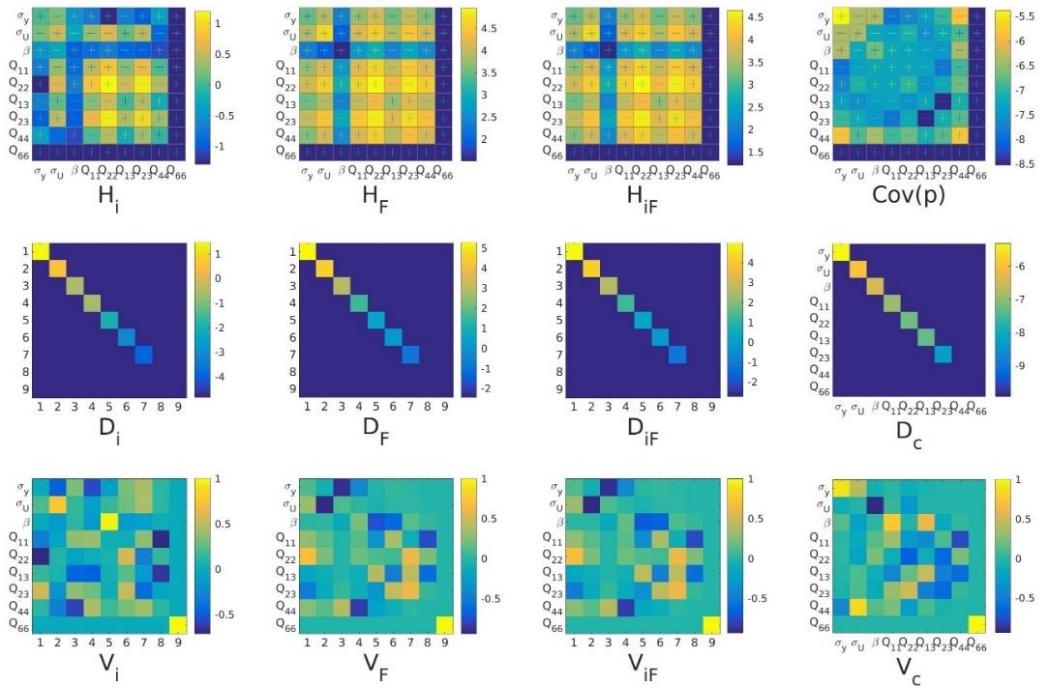

Figure 12 - Absolute image, force, total Hessians and the corresponding parameter covariance matrix (log_{10} scale, first row), with their diagonal matrices (log_{10} scale, second row) and eigenvectors (third row).

Furthermore, the covariance matrix of the calibrated parameters is also reported and used to obtain an evaluation of the identification uncertainties due to measurement uncertainties. A first order analysis is to consider the square root of the diagonal elements of the covariance matrix (i.e., individual dimensionless standard uncertainties) and then multiply them by the value of the identified parameters since the computations were conducted using dimensionless parameters (Table 3). The uncertainties are low due to the high sensitivities and good experimental conditions.

The elastic parameters calibrated in the elastic regime and those calibrated in the elastoplastic regime were different (especially using the orthotropic model) indicating that some elements already yielded in the elastic domain but were not taken into account in the elastic model. As expected, the parameter Q_{11} had systematically higher values than Q_{22} because of the orientation of the filament, and the anisotropy generated by the existence of weld lines and air gaps. Even though the elastic parameters found using isotropic and orthotropic models were quite different, the final residuals were very close. Further, the values of the identified yield stress were close, and those of the hardening coefficient β did not evolve much, which was due to its low sensitivity. There was a small difference in the yield stress found using isotropic or orthotropic elasticity. Moreover, the identified ultimate strength (29 MPa) was higher than that

reported by Lanzillotti *et al.* [42] (i.e., 23-25 MPa). More details on this comparison are discussed in Section 5.

Even though the FEMU-F results were in very good agreement with I-DIC in the analyzed case (orthotropic elasticity and plasticity), they are only considered as a good approximation of the final results since the model was not probed against images. The results of FEMU-F can thus be used as initialization for I-DIC computations since FEMU-F requires a shorter computation time (no image residuals are needed).

Table 3 - Identified parameters using different constitutive models and image sets, element length = 5px

Regime	Elastic (images 51-111)				Elastoplastic (images 51-211)					
Model	Isotropic I-DIC		Orthotropic I-DIC		Isotropic I-DIC		Orthotropic I-DIC		Orthotropic FEMU-F	
	Value	Uncertainty	Value	Uncertainty	Value	Uncertainty	Value	Uncertainty	Value	Uncertainty
E(MPa)	1430	2	—	—	1418	1	—	—	—	—
ν	0.22	10^{-3}	—	—	0.28	$2\ 10^{-5}$	—	—	—	—
σ_y(MPa)	—	—	—	—	16	0.05	19	0.04	18	0.03
σ_U(MPa)	—	—	—	—	29	0.02	28	0.02	28	0.01
β	—	—	—	—	95	0.1	100	0.05	100	0.03
Q_{11}(MPa)	1635	—	2489	0.9	1823	—	2414	0.6	2411	0.3
Q_{22}(MPa)	1635	—	1586	1.1	1823	—	1670	0.5	1671	0.4
Q_{13}(MPa)	464	—	1176	0.5	718	—	1224	0.3	1229	0.2
Q_{23}(MPa)	464	—	1467	1.3	718	—	1364	0.4	1362	0.3
Q_{44}(MPa)	586	—	1090	3.5	553	—	870	1.1	879	0.8
Q_{66}(MPa)	586	—	500	—	553	—	500	—	500	—

3.1.4. Application with Additional Images

One additional study is to probe the elastoplastic model and use it on images beyond the calibration range (images 51-211) and up to the peak load (images 51-251). Such analysis may allow us to detect damage and crack propagation, which appeared in the *y*-displacement difference (Figure 13).

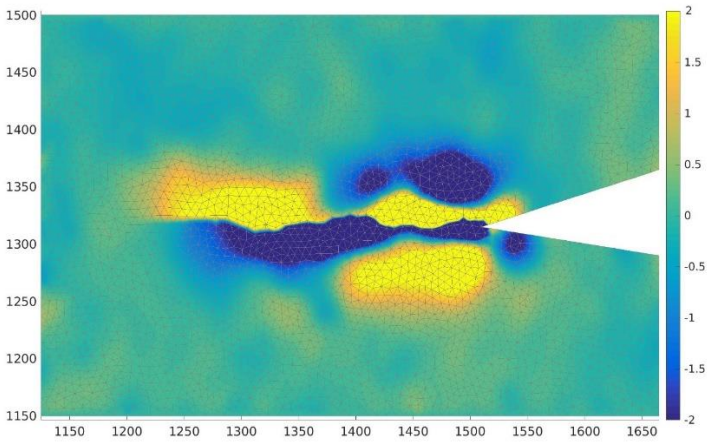

Figure 13 - Difference of y-displacement fields (y_{FEM} - y_{DIC}) indicating crack propagation at maximum load (image 251), element length = 5px.

When considering the instantaneous residuals of image, load and displacement fields (Figure 14), they have low values in the elastic domain (images 51-111, i.e., very small model errors). However, near image 111, the image residual (Figure 14(a)) started to increase along with the displacement ones (Figure 14(c-d)), thereby indicating that yielding occurred, and that the identification was becoming less satisfactory (elastoplastic regime). In the elastoplastic phase, the gray level residuals of DIC and I-DIC started to separate, which is due to model errors. The force residual, however, had smaller levels compared to the elastic phase (Figure 14(b)), because of its high sensitivity to the ultimate strength and plasticity activation. Near image 211, all residuals started to increase considerably, thereby indicating that another mechanism was not accounted for (i.e., damaged zones were detected). Since damage was not modeled, the model errors could not be lowered and the residuals increased drastically. Further, the initial force fluctuations are still due to the fact that measured displacements were applied as boundary conditions to the numerical simulations.

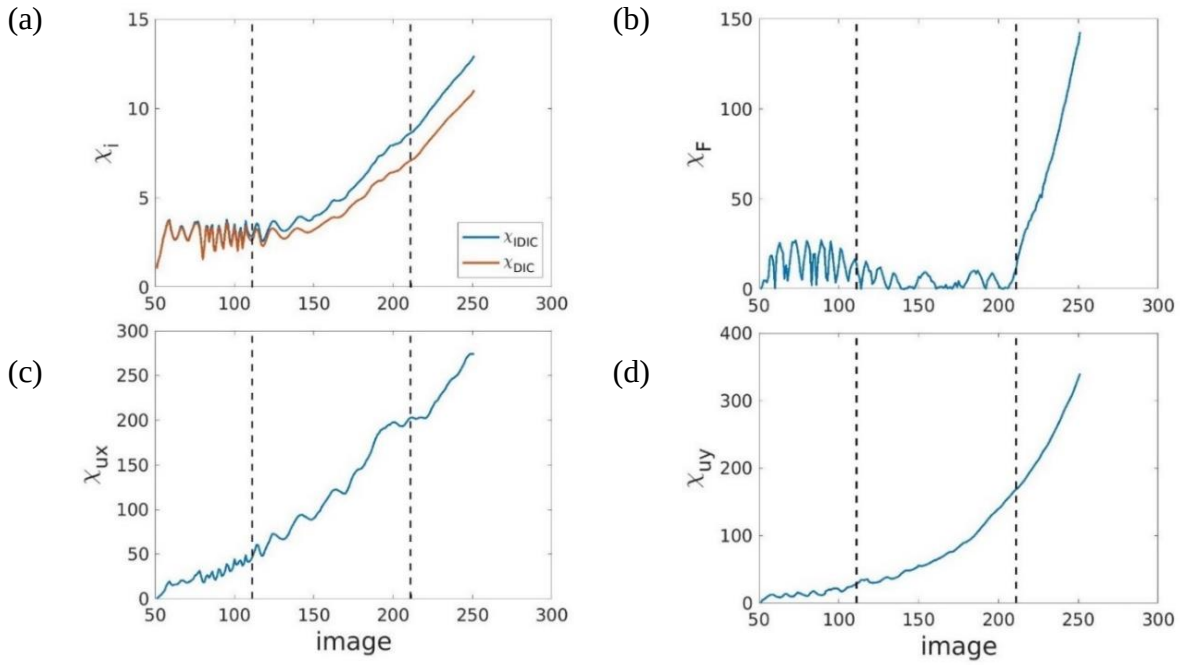

Figure 14 - Instantaneous image (a), force (b) and displacement (c-d) residuals as functions of the image number. The dashed vertical lines depict the transitions between the elastic, elastoplastic and damage regimes.

Since the conducted experiment may also be used to quantify crack propagation, mesoscopic images (local view, high resolution, back face of the specimen, see Figure 2(a)) were acquired simultaneously along with the macroscopic pictures (global view, which was used in the identification procedure, front face of the specimen). However, these mesoscopic images could not be directly used in the identification procedure since they did not capture the right and left edges of the sample (blue mesh, Figure 15). Therefore, the resultant force could not be computed. A comparison between the two meshes in the macroscopic (white) and mesoscopic (blue) cases is shown in Figure 15 in which the ROI of the mesoscopic mesh was redrawn at the macroscopic scale (i.e., 1 px of macroscopic images corresponded to 3.82 px for mesoscopic acquisitions).

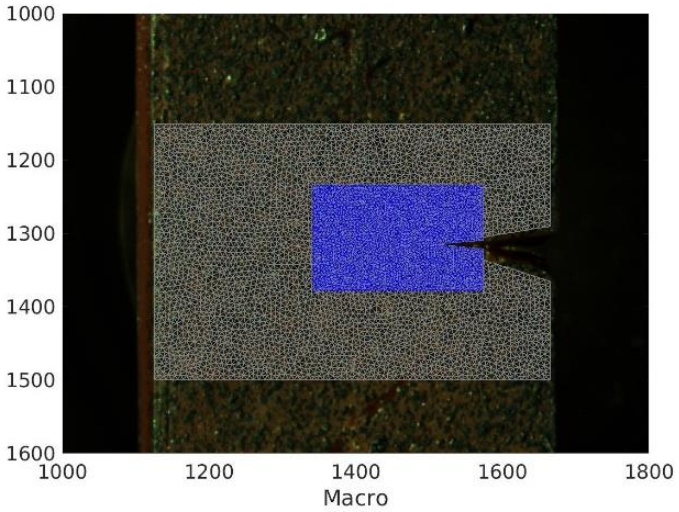

Figure 15 - Meshes used in mesoscopic (blue, 10px-elements at the mesoscale) and macroscopic (white, 5px-elements of the macroscale) DIC analyses. Scale: 1 macroscopic px ≡3.82 mesoscopic px.

These images were used to further probe the relevance of the calibrated parameters. The mesoscopic mesh is shown in Figure 16 at the mesoscale. The nodes on the upper, lower, right and left edges were selected since they were not free edges (which was not the case for the two segments around the notch root), and the displacement of the selected modes were obtained using DIC measurements.

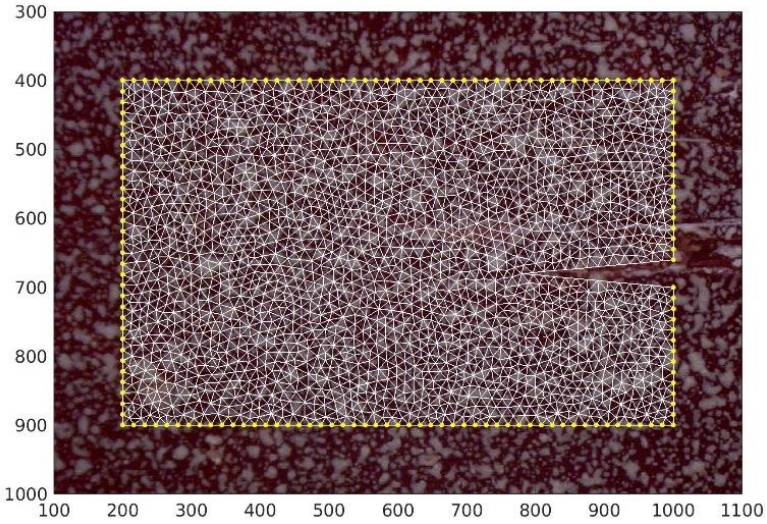

Figure 16 - Mesoscale mesh in white and boundary nodes in yellow, element length = 10 px.

The previously calibrated parameters using macroscopic images were utilized in order to estimate the image residuals using mesoscopic images. All images before the peak load (51-251) were used in the present analysis. The results are different from those obtained at the

macroscale for two reasons: (i) the high resolution of this image set compared to the macroscopic data, and (ii) the fact that the mesoscopic images were acquired on the other face of the sample, and hence, did not monitor exactly the same physical surface. The quantitative results are reported in Table 4 for elastic (images 51-111), elastoplastic (images 51-211, by extrapolation) and damaged (images 51-251, by extrapolation) regimes (Table 4). The same computations were also conducted using the results of elastoplastic analyses (using images 51-211).

In the elastic domain, the residuals were extremely close for all models (the differences were less than 0.01, essentially negligible). As seen previously, an isotropic elastic model was a very good compromise in this regime. In the elastoplastic domain, the residuals using elastic models were higher compared to those using elastoplastic laws due to model errors. Comparing isotropic and orthotropic models suggests that the difference is negligible. The same result was also found for the damage regime but with relatively higher values of residuals. These higher levels were due to damage occurring in this regime. Thus, the results with the isotropic elastoplastic model are deemed optimal since they represent a very good compromise between low total residual ($\chi_{tot} = 1.34$) and shorter computation time.

Table 4 - Residuals using different constitutive models and image sets, element length = 10px. The bold cells indicate that the residual was computed for calibration range

Regime	Elasticity (images 51-111)		Elastoplasticity (images 51-211)	
Model	Isotropic	Orthotropic	Isotropic	Orthotropic
χ_i (Images 51-111)	**1.05**	**1.05**	1.05	1.05
χ_i (Images 51-211)	1.5	1.5	**1.34**	**1.36**
χ_i (Images 51-251)	1.9	1.9	1.57	1.6

When considering the instantaneous displacement residuals (Figure 17), they had low values in the elastic domain (images 51-111, i.e., very small model error). However, near image 100, the residuals started to increase indicating that yielding had occurred (elastoplastic regime). Near image 211, the residuals increased even more due to damaged zones. The observed oscillations are much smaller in the present case than those observed in the macroscopic analyses (Figure 17(b)).

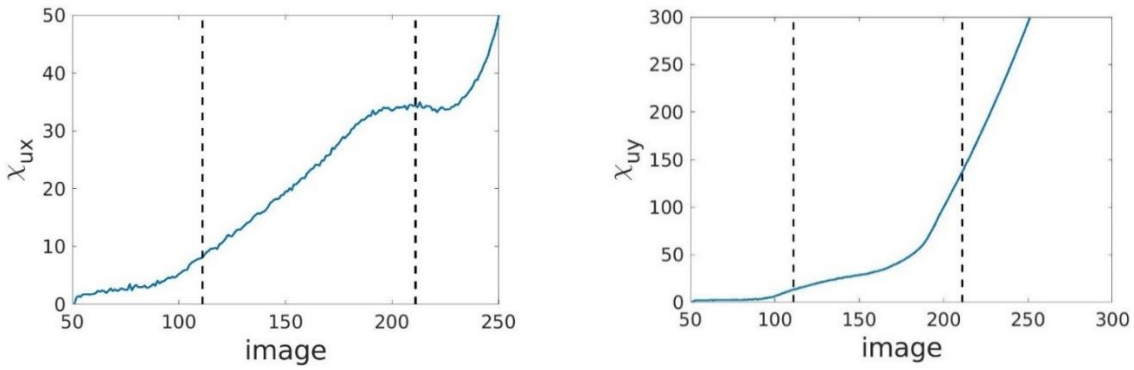

(a) (b)

Figure 17 - Instantaneous displacement residuals as functions of image number. The dashed vertical lines depict the transitions between the elastic, elastoplastic and damage regimes.

The instantaneous image residual (Figure 18(a)) had low levels in the elastic domain (images 51-111). It then started to increase near image 100 (due to yielding), and then increased even more after image 211 because of damage. This earlier effect was due to the high resolution of mesoscopic images, which allowed plasticity and damage to be observed much closer as seen in the *y*-displacement difference field in Figure 18(b).

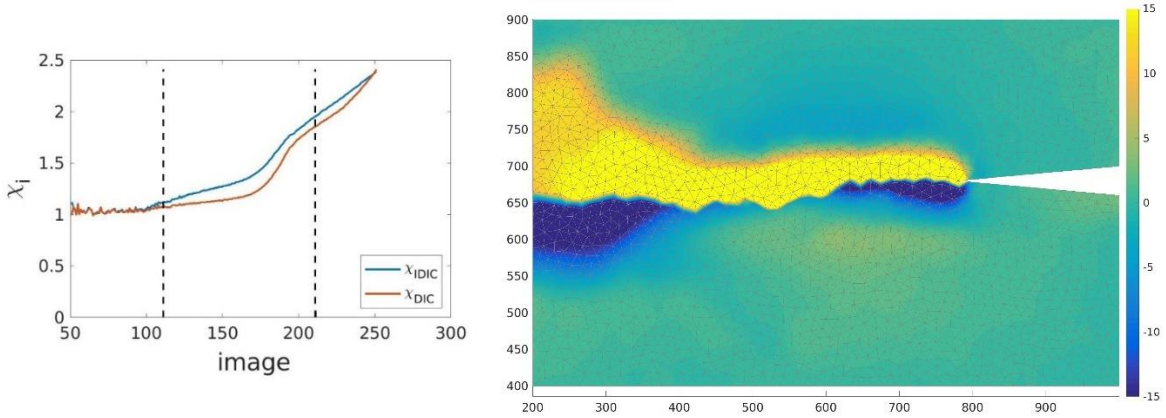

(a) (b)

Figure 18 - (a) Instantaneous image residual as a function of image number. The dashed vertical lines depict the transitions between elastic, elastoplastic and damage regimes.

(b) Difference of y-displacement fields (y_{FEM} - y_{DIC}) indicating crack propagation at maximum load on mesoscopic images (image 251), element length = 10px.

3.2. Oriented deposition

The identification strategy for the optimized SENT specimen was similar to that conducted on the ± 45° sample. However, the material orientations had to be specified for each element of the mesh. The angle for each point of printing contours (Figure 19) was determined from the information in the G-code. The center of gravity of each element was determined, and then the

nearest point of the contour was determined and its angle was assigned to the considered element. In the material frame, the sought parameters were assumed to be identical everywhere.

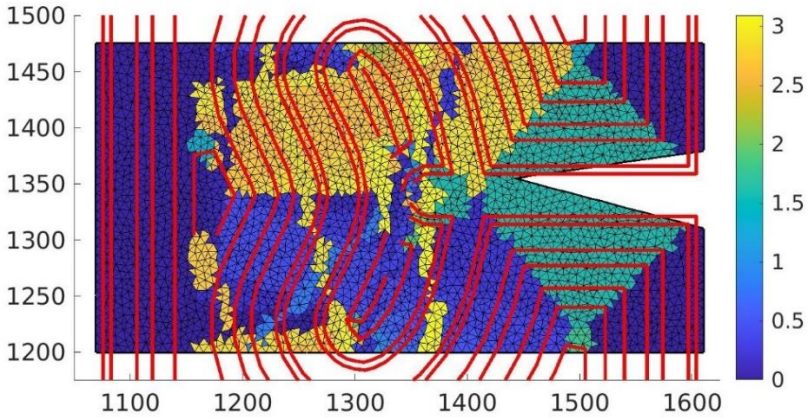

Figure 19 - Mesh for the optimized SENT specimen showing the different material orientations [rad]. The printing contours (red lines) are overlaid, element length = 5px.

I-DIC was then run again and after convergence, the total residuals were minimized for an elastoplastic model with anisotropic elasticity (Figure 20*Figure 20 - Changes in total residuals (a), corrections on dimensionless parameters (b), and dimensionless parameters (c) as functions of iteration number showing the convergence of I-DIC using an orthotropic elastoplastic model.*

(a)). The initial parameters were those of the final identification of the ± 45° configuration except for the yield stress, which was set to 14.5 MPa, and the ultimate strength to 38 MPa in order to ensure rapid convergence of the code. Figure 20(b) shows how the parameter corrections decreased to small values at convergence, and the changes of dimensionless parameters are displayed in Figure 20(c). Only two iterations were required, thereby indicating that the identified elastic parameters using the optimized specimen were very close to those calibrated for the ± 45° configuration.

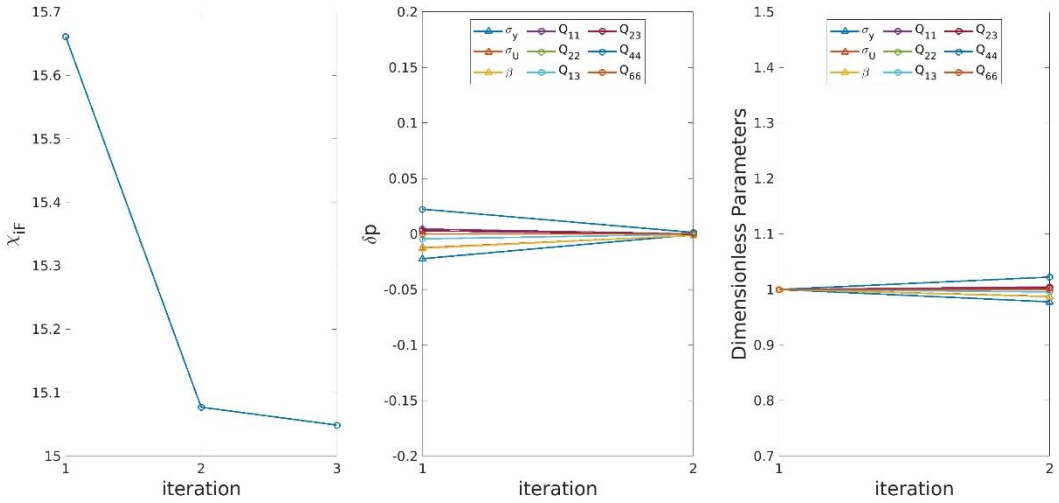

(a) (b) (c)

Figure 20 - Changes in total residuals (a), corrections on dimensionless parameters (b), and dimensionless parameters (c) as functions of iteration number showing the convergence of I-DIC using an orthotropic elastoplastic model.

The different instantaneous residuals as functions of image number are reported in Figure 21. As previously, two regimes were observed (notably on the image and force data), namely, a first elastic regime (images 11-51) and then an elastoplastic domain (images 51-171). During the elastic phase, the gray level residuals of DIC and I-DIC (Figure 21(a)) remained very close but not equal. A small gap between both residuals was seen in the elastoplastic phase, and increased more, presumably because of damage that was not modeled. This trend was also associated with drastic increases in displacement residuals (Figure 21(c-d)). Conversely, the force residual (Figure 21(b)) fluctuated in the elastic phase (for the same reasons as before) and then had a different trend in the elastoplastic regime. Its overall levels remained similar in both phases.

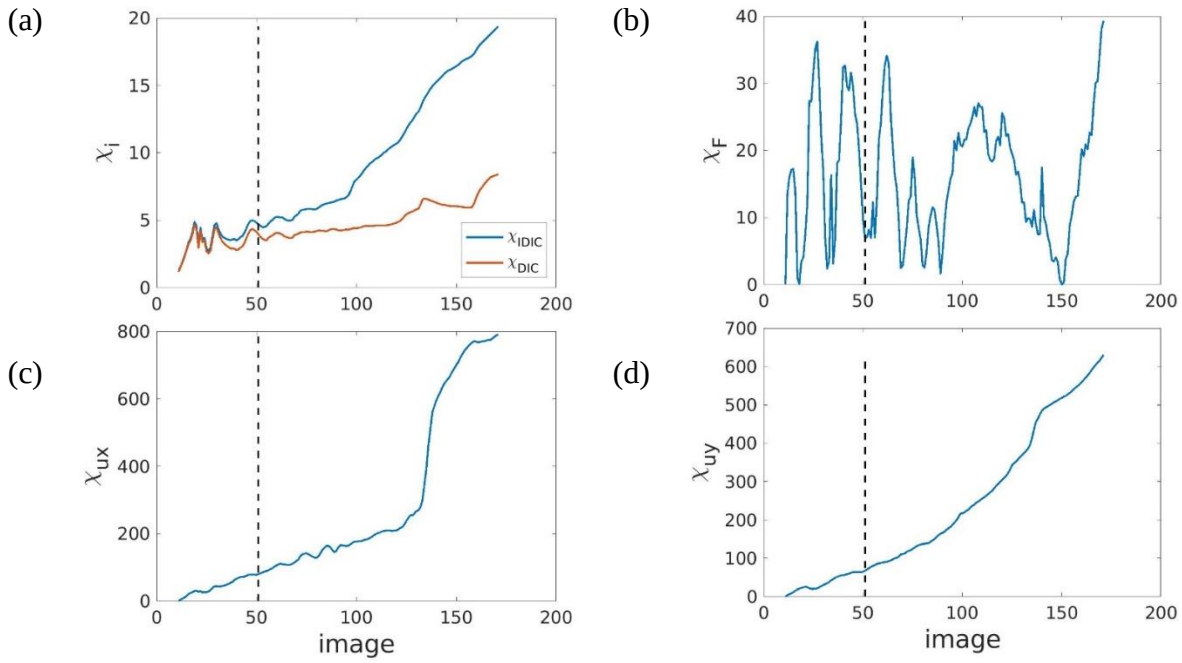

Figure 21 - Instantaneous image (a), force (b) and displacement (c-d) residuals as functions of image number. The dashed vertical lines depict the transitions between the elastic and elastoplastic regimes.

The total residuals using different models are reported in Table 5. In the elastic regime, the difference between isotropic and orthotropic descriptions was vanishingly small compared to the needed computation time, which was already observed in the previous analyses. In the elastoplastic regime, three elasticity descriptions were tested: isotropic, orthotropic in the ± 45° orientation, and orthotropic with varying orientations following the printing contours

(optimized architecture). The global residual decreased as the number of parameters increased. Yet, this decay remained very modest in comparison to the increase in number of material parameters (from 5 to 9). It is noteworthy that even though the number of parameters in the ± 45° and optimized configurations were the same, the global residual in the optimized case was slightly smaller. The negligible difference between the residuals with the three analyzed elastic descriptions again suggests that isotopic elasticity is very good representation of the material behavior.

Table 5 - Global residuals using different constitutive models in the elastic and elastoplastic regimes, element length = 5px

Regime	Elastic (images 11-51)		Elastoplastic (images 11-171)		
Model	Isotropic	Orthotropic optimized	Isotropic	Orthotropic ±45°	Orthotropic optimized
χ_{iF}	**9.8**	**9.8**	**16.4**	**15.1**	**15.0**

Table 6 gathers the values of the identified parameters for the investigated models in the two regimes. Each identified parameter is reported along with its standard uncertainty (obtained, as previously, from the estimated covariance matrix). The uncertainties were still very low. The elastic parameters calibrated in the elastic regime, and those calibrated in the elastoplastic regime were close. The parameter Q_{11} was again systematically greater than Q_{22}. The values of the yield stress and hardening coefficient β were slightly lower for the isotropic case than for orthotropic elasticity. The elastic parameters in the orthotropic cases (± 45° and optimized) in the elastoplastic regime were very close (difference less than 10%) even though the orientations of the elements were completely different. This result reinforces the statement that the generated anisotropy in material extrusion was negligible in the studied cases.

Table 6 - Identified parameters using different constitutive models, element length = 5px

Regime	Elastic (images 11-51)				Elastoplastic (images 11-171)					
Model	Isotropic		Orthotropic optimized		Isotropic		Orthotropic ± 45°		Orthotropic optimized	
	Value	Uncertainty	Value	Uncertainty	Value	Uncertainty	Value	Uncertainty	Value	Uncertainty
E(MPa)	1213	1	—	—	1137	0.8	—	—	—	—
ν	0.29	$2\ 10^{-4}$	—	—	0.29	10^{-4}	—	—	—	—
σ_y(MPa)	—	—	—	—	10	0.02	13	$3\ 10^{-3}$	14	$3\ 10^{-3}$
σ_U(MPa)	—	—	—	—	35	0.03	37	0.02	37	0.02
β	—	—	—	—	75	0.07	98	0.01	97	0.01
Q_{11}(MPa)	1591	—	2387	0.4	1470	—	2375	0.3	2511	0.3
Q_{22}(MPa)	1591	—	1602	0.7	1470	—	1554	0.2	1579	0.2
Q_{13}(MPa)	651	—	1238	0.2	585	—	1246	0.1	1294	0.1
Q_{23}(MPa)	651	—	1414	0.5	585	—	1455	0.1	1534	0.1
Q_{44}(MPa)	470	—	867	0.5	443	—	904	0.2	947	0.2
Q_{66}(MPa)	470	—	500	—	443	—	500	—	500	—

4. Discussion

The difference in elastic properties between the ± 45° and optimized specimens are attributed to bigger air gaps between the filaments in the optimized specimen (Figure 22Figure 22 - Reference pictures of (a) the specimen with ± 45° orientation, and (b) optimized orientation. The width of the samples was equal to 8 mm

), which induced lower Young's moduli in the latter case. In the optimized specimen, the filament deposition followed the principal stress directions. It resulted in circular trajectories

that led to higher amounts of porosities in the material bulk because of infill challenges. These porosities affected the elastic properties of such fabricated configurations [43]. By varying the physical conditions (build-platform temperature, infill strategy), configurations with different amounts porosity in the volume may thus be obtained.

Even though the elastic properties were different, the plastic properties between both specimens were close. The ultimate strength in the optimized case was higher than that in the ± 45° orientation since many filaments in the optimized case were aligned in the longitudinal direction (Figure 22). Such trend was not anticipated from the macroscopic response of both samples (Figure 4). In specimens obtained by extrusion with external contour(s) and an inner core exhibit different mechanical responses [44]. FFF samples show the best tensile performance in the longitudinal direction. This tendency was also observed in the present study.

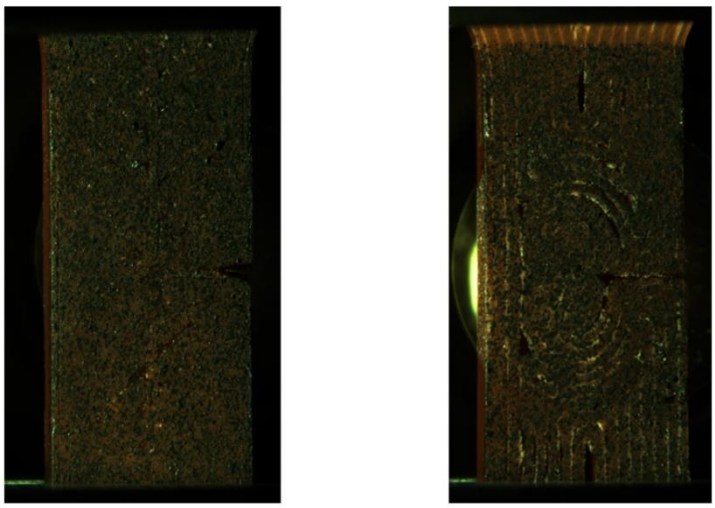

(a) (b)

Figure 22 - Reference pictures of (a) the specimen with ± 45° orientation, and (b) optimized orientation. The width of the samples was equal to 8 mm

Lanzillotti et al. [42] conducted tensile experiments using a specimen with 45° and longitudinal configurations (Figure 23(a-b)). Their results showed a first elastic phase followed by an elastoplastic regime in agreement with what was observed herein. At a strain level of approximately 2%, the stress level started to plateau, and the ultimate strength was equal to 24 MPa in the 45° case, and 33 MPa in the longitudinal orientation (Figure 23((a-b)). These values of ultimate strength are consistent with those identified using the ± 45° specimen (28-29 MPa, see Table 3) and those using the optimized one (36 MPa, see Table 6). It is worth noting that this result cannot be directly compared with the experimental net section stress-global strain

plot (Figure 3) since the strain field was not uniform in the present analyses. This difference is observed for the maximum strain of Figure 3 (≈ 0.1%) compared to Figure 23(b) (≈ 4.5%).

The previous comparison should thus be performed with a simulation of a tensile test on an *unnotched specimen* using the identified parameters. A final analysis was conducted using the results of the elastoplastic model in order to get the response of a volume element (corresponding to the macroscopic response of a material point subjected to uniaxial tension) in a simple tensile loading. The simulation was conducted with 1-mm thick plane stress CPS3 elements. The tensile loading was prescribed along the vertical direction and the final strain level was set to 10%. Four simulations were conducted using two models: isotropic and orthotropic elasticity, and the calibrated elastoplastic parameters in each experiment: ± 45°-oriented filaments and optimized deposition (Figure 23(c-d)). The different stress/strain responses are compared to the results of Lanzillotti et al. [42]. The fact that the chosen elastoplastic model had very marginal influence on the results further validates the use of an isotropic elastoplastic law. The ultimate strength in the optimized orientation was higher than that in the ± 45° case (Table 3 and Table 6). This difference is observed in the experimental plots (Figure 23(a-b)) and in the simulated ones (Figure 23(c-d)). In this last configuration, the role of the external contours (in samples with no notch), which led to an enhanced mechanical response, is confirmed. The difference between the simulated results and the experimental data of Lanzillotti et al. [42] is small. Hence, the calibrated parameters are deemed validated.

(a)

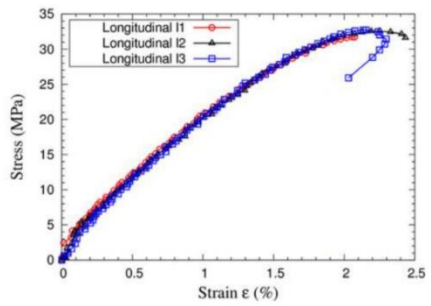

(b)

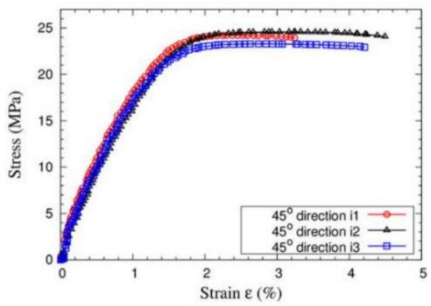

(c)

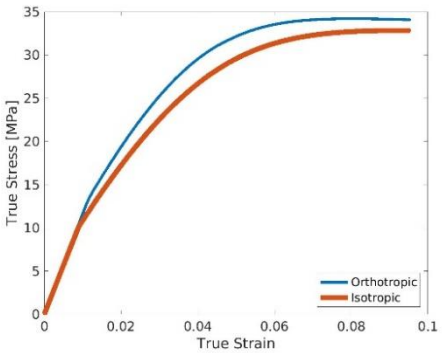

(d)

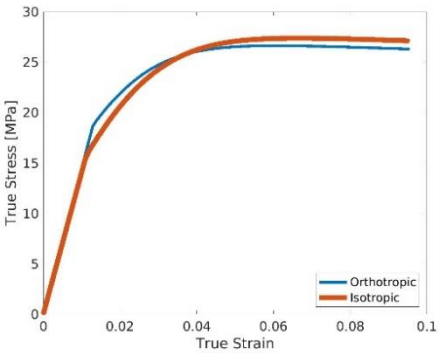

Figure 23 - Stress/strain plots of tensile experiments with (a) longitudinal and (b) 45°-oriented filaments [42]. True stress vs. true strain of tensile simulations using the calibrated parameters of the (c) optimized specimen and (d) ±45° specimen. The small difference between the responses using isotropic or orthotropic elasticity validates the conclusion of weak elastic anisotropy.

5. Conclusion

It was shown that exploiting the data extracted from a *single* SENT specimen enabled material parameters to be calibrated via integrated DIC even in anisotropic elasticity. Several models were investigated (elastic and elastoplastic laws) in order to quantify the impact of elastic anisotropy of printed layers on the mechanical response of ABS manufactured via material extrusion (isotropic, ± 45° orthotropic and optimized orthotropic models). The best compromise was found for an isotropic elastoplastic model. The predictions with an orthotropic elastoplastic model only slightly reduced the global residuals, and the differences were considered insignificant. Besides, the computation time was doubled when more parameters had to be calibrated, thus making the use of such enriched models even less appealing. The same conclusion was drawn for both printed orientations. Further, in the optimized configuration, accounting for the local orientation did not improve the results in comparison to ± 45°-oriented filaments. This result further suggested that isotropic elasticity was a very good first order approximation in the investigated cases. Conversely, the yield stress and ultimate strengths were different in both cases. This observation hints at enriching the selected model to account for plasticity anisotropy (e.g., Hill model [45]).

The identification procedure required some preparations and pre-computations before launching complete and precise calibrations. Notably, exploiting DIC results (gray level residual maps) to determine the analysis range, estimating the image, displacement and force standard uncertainties, conducting several computations using coarse meshes to approximate the solution at convergence, estimating the identifiability of the material parameters and checking whether the investigated solution corresponded to a local or global minimum. Deducing the orientation of each element in the case of optimized deposition was also required before launching the code. Once these pre-computations were carried out, complete computations were run with fine meshes to obtain the final results. This step was followed by estimating the uncertainties associated with each calibrated parameter using their covariance matrix, and the evaluation of their identifiability using the total Hessian at convergence.

The final step of this work was to use the calibrated parameters and conduct simulations of simple tensile tests. These simulations were used to compare the corresponding stress-strain

curves to others reported in the literature. The comparison was rather consistent with small differences in terms of ultimate strength.

References

[1] I. Gibson, D. Rosen, B. Stucker, M. Khorasani, Additive Manufacturing Technologies, 2021. https://doi.org/10.1007/978-3-030-56127-7.

[2] T.D. Ngo, A. Kashani, G. Imbalzano, K.T.Q. Nguyen, D. Hui, Additive manufacturing (3D printing): A review of materials , methods , applications and challenges, Compos. Part B. 143 (2018) 172–196. https://doi.org/10.1016/j.compositesb.2018.02.012.

[3] J. Chang, J. He, M. Mao, W. Zhou, Q. Lei, X. Li, D. Li, C.K. Chua, X. Zhao, Advanced material strategies for next-generation additive manufacturing, Materials (Basel). 11 (2018). https://doi.org/10.3390/ma11010166.

[4] S.A.M. Tofail, E.P. Koumoulos, A. Bandyopadhyay, S. Bose, L. O'Donoghue, C. Charitidis, Additive manufacturing: scientific and technological challenges, market uptake and opportunities, Mater. Today. 21 (2018) 22–37. https://doi.org/10.1016/j.mattod.2017.07.001.

[5] A. Zhakeyev, P. Wang, L. Zhang, W. Shu, H. Wang, J. Xuan, Additive Manufacturing: Unlocking the Evolution of Energy Materials, Adv. Sci. 4 (2017). https://doi.org/10.1002/advs.201700187.

[6] K.S. Boparai, R. Singh, Advances in Fused Deposition Modeling, Ref. Modul. Mater. Sci. Mater. Eng. (2017) 1–10. https://doi.org/10.1016/b978-0-12-803581-8.04166-7.

[7] S.A.M. Tofail, E.P. Koumoulos, A. Bandyopadhyay, S. Bose, L. O'Donoghue, C. Charitidis, Additive manufacturing: scientific and technological challenges, market uptake and opportunities, Mater. Today. 21 (2018) 22–37. https://doi.org/10.1016/j.mattod.2017.07.001.

[8] R.J. Zaldivar, D.B. Witkin, T. Mclouth, D.N. Patel, K. Schmitt, J.P. Nokes, Influence of Processing and Orientation Print Effects on the Mechanical and Thermal Behavior of 3D-Printed ULTEM® 9085 Material, (2016). https://doi.org/10.1016/j.addma.2016.11.007.

[9] S.H. Ahn, M. Montero, D. Odell, S. Roundy, P.K. Wright, Anisotropic material properties of fused deposition modeling ABS, 2002. https://doi.org/10.1108/13552540210441166.

[10] I. Rivet, N. Dialami, M. Cervera, M. Chiumenti, G. Reyes, M.A. Pérez, Experimental, computational, and dimensional analysis of the mechanical performance of fused filament fabrication parts, Polymers (Basel). 13 (2021) 1–18. https://doi.org/10.3390/polym13111766.

[11] S. Ahn, M. Montero, D. Odell, S. Roundy, P.K. Wright, Anisotropic material properties of fused deposition modeling ABS, Rapid Prototyp. J. 8 (2002) 248–257. https://doi.org/10.1108/13552540210441166.

[12] M. Samykano, S.K. Selvamani, K. Kadirgama, W.K. Ngui, G. Kanagaraj, K. Sudhakar, Mechanical property of FDM printed ABS: influence of printing parameters, Int. J. Adv. Manuf. Technol. 102 (2019) 2779–2796. https://doi.org/10.1007/s00170-019-03313-0.

[13] D. Popescu, A. Zapciu, C. Amza, F. Baciu, R. Marinescu, FDM process parameters influence over the mechanical properties of polymer specimens: A review, Polym. Test. 69 (2018) 157–166. https://doi.org/10.1016/j.polymertesting.2018.05.020.

[14] C. Koch, L. Van Hulle, N. Rudolph, Investigation of mechanical anisotropy of the fused filament fabrication process via customized tool path generation, Addit. Manuf. 16 (2017) 138–145.

[15] Y. Xia, K. Xu, G. Zheng, R. Zou, B. Li, P. Hu, Investigation on the elasto-plastic constitutive equation of parts fabricated by fused deposition modeling, Rapid Prototyp. J. 3 (2019) 592–601. https://doi.org/10.1108/RPJ-06-2018-0147.

[16] E. Cuan-Urquizo, E. Barocio, V. Tejada-Ortigoza, R. Byron Pipes, C.A. Rodriguez, A. Roman-flores, Characterization of the Mechanical Properties of FFF Structures and Materials : A Review on the Theoretical Approaches, Materials (Basel). 12 (2019) 1–25. https://doi.org/10.3390/ma12060895.

[17] K.T. KAVANAGH, R.W. CLOUGH, Finite element applications in the characterization of elastic solids, Int. J. Solids Struct. 7 (1971) 11–23.

[18] D. Claire, F. Hild, S. Roux, A finite element formulation to identify damage fields: The

equilibrium gap method, Int. J. Numer. Methods Eng. 61 (2004) 189–208. https://doi.org/10.1002/nme.1057.

[19] F. Mathieu, H. Leclerc, F. Hild, S. Roux, Estimation of Elastoplastic Parameters via Weighted FEMU and Integrated-DIC, Exp. Mech. 55 (2015) 105–119. https://doi.org/10.1007/s11340-014-9888-9.

[20] P. Meißner, H. Watschke, J. Winter, T. Vietor, Artificial neural networks-based material parameter identification for numerical simulations of additively manufactured parts by material extrusion, Polymers (Basel). 12 (2020) 1–28. https://doi.org/10.3390/polym12122949.

[21] M. Grédiac, E. Toussaint, F. Pierron, Special virtual fields for the direct determination of material parameters with the virtual fields methods. 1 - Principle and definition, Int. J. Solids Struct. 39 (2002) 2691–2705. https://doi.org/10.1016/S0020-7683(02)00127-0.

[22] S. Avril, M. Grédiac, F. Pierron, Sensitivity of the virtual fields method to noisy data, Comput. Mech. 34 (2004) 439–452. https://doi.org/10.1007/s00466-004-0589-6.

[23] A. Marek, F.M. Davis, F. Pierron, Sensitivity-based virtual fields for the non-linear virtual fields method, Comput. Mech. 60 (2017) 409–431. https://doi.org/10.1007/s00466-017-1411-6.

[24] J. Réthoré, Muhibullah, T. Elguedj, M. Coret, P. Chaudet, A. Combescure, Robust identification of elasto-plastic constitutive law parameters from digital images using 3D kinematics, Int. J. Solids Struct. 50 (2013) 73–85. https://doi.org/10.1016/j.ijsolstr.2012.09.002.

[25] S. Avril, F. Pierron, General framework for the identification of constitutive parameters from full-field measurements in linear elasticity, Int. J. Solids Struct. 44 (2007) 4978–5002. https://doi.org/10.1016/j.ijsolstr.2006.12.018.

[26] M.B.R. Bertin, F. Hild, S. Roux, Optimization of a Cruciform Specimen Geometry for the Identification of Constitutive Parameters Based Upon Full-Field Measurements, Strain. 52 (2016) 307–323. https://doi.org/10.1111/str.12178.

[27] J. Neggers, F. Mathieu, F. Hild, S. Roux, N. Swiergiel, Improving full-field identification using progressive model enrichments, Int. J. Solids A. 119 (2017) 213–

223. https://doi.org/10.1016/j.ijsolstr.2017.03.013.

[28] J. Neggers, F. Mathieu, F. Hild, S. Roux, Simultaneous full-field multi-experiment identification, Mech. Mater. 133 (2019) 71–84. https://doi.org/10.1016/j.mechmat.2019.03.001.

[29] J.C. Passieux, F. Bugarin, C. David, J.N. Périé, L. Robert, Multiscale Displacement Field Measurement Using Digital Image Correlation: Application to the Identification of Elastic Properties, Exp. Mech. 55 (2015) 121–137. https://doi.org/10.1007/s11340-014-9872-4.

[30] J. Remacle, J. Lambrechts, B. Seny, Blossom-Quad: A non-uniform quadrilateral mesh generator using a minimum-cost perfect-matching algorithm, International. (2012) 1102–1119. https://doi.org/10.1002/nme.

[31] S. Roux, F. Hild, Optimal procedure for the identification of constitutive parameters from experimentally measured displacement fields, Int. J. Solids Struct. 184 (2020) 14–23. https://doi.org/10.1016/j.ijsolstr.2018.11.008.

[32] J. Gardan, A. Makke, N. Recho, Improving the fracture toughness of 3D printed thermoplastic polymers by fused deposition modeling, Int. J. Fract. 210 (2018) 1–15. https://doi.org/10.1007/s10704-017-0257-4.

[33] S. Paul, Finite element analysis in fused deposition modeling research: A literature review, Measurement. 178 (2021). https://doi.org/10.1016/j.measurement.2021.109320.

[34] J. Gardan, A. Makke, N. Recho, Fracture Improvement by Reinforcing the Structure of Acrylonitrile Butadiene Styrene Parts Manufactured by Fused Deposition Modeling, 3D Print. Addit. Manuf. (2018) 3dp.2017.0039. https://doi.org/10.1089/3dp.2017.0039.

[35] J. Marae Djouda, D. Gallittelli, M. Zouaoui, A. Makke, J. Gardan, N. Recho, J. Crépin, Local scale fracture characterization of an advanced structured material manufactured by fused deposition modeling in 3D printing, Frat. Ed Integrita Strutt. 14 (2020) 534–540. https://doi.org/10.3221/IGF-ESIS.51.40.

[36] J. Marae Djouda, M.A. Bouaziz, M. Zouaoui, M. Rambaudon, J. Gardan, N. Recho, J. Crépin, Experimental approach for microscale mechanical characterization of polymeric structured materials obtained by additive manufacturing, Polym. Test. 89 (2020). https://doi.org/10.1016/j.polymertesting.2020.106634.

[37] F. Hild, S. Roux, Digital Image Correlation, in: P. Rastogi, E. Hack (Eds.), Opt. Methods Solid Mech. A Full-f. Approach, EDS, Wiley-VCH, Weinheim, Germany, 2012: pp. 183–228.

[38] G. Besnard, F. Hild, S. Roux, "Finite-element" displacement fields analysis from digital images: Application to Portevin-Le Châtelier bands, Exp. Mech. 46 (2006) 789–803. https://doi.org/10.1007/s11340-006-9824-8.

[39] H. Leclerc, J.-N. Périé, S. Roux, F. Hild, Integrated Digital Image Correlation for the Identification of Mechanical Properties, in: A. Gagalowicz, W. Philips (Eds.), Springer Berlin Heidelberg, 2009: pp. 161–171. https://doi.org/doi.org/10.1007.

[40] E. Voce, The relationship between stress and strain for homogeneous deformation, J. Inst. Met. 74 (1948) 537–562.

[41] H. Leclerc, J. Neggers, F. Mathieu, F. Hild, S. Roux, Correli 3.0, IDDN. FR. 001.520008. 000. SP 2015.000. 31500, 2015.

[42] P. Lanzillotti, J. Gardan, A. Makke, N. Recho, Enhancement of fracture toughness under mixed mode loading of ABS specimens produced by 3D printing, Rapid Prototyp. J. 25 (2019) 679–689. https://doi.org/10.1108/RPJ-09-2018-0247.

[43] Y. Liao, C. Liu, B. Coppola, G. Barra, L. Di Maio, L. Incarnato, K. Lafdi, Effect of Porosity and Crystallinity on 3D Printed PLA Properties, Polymers (Basel). 11 (2019) 1–14.

[44] N. Dialami, M. Chiumenti, M. Cervera, R. Rossi, U. Chasco, M. Domingo, Numerical and experimental analysis of the structural performance of AM components built by fused filament fabrication, Int. J. Mech. Mater. Des. 17 (2021) 225–244. https://doi.org/10.1007/s10999-020-09524-8.

[45] R. Hill, A Theory of the Yielding and Plastic Flow of Anisotropic Metals, Proceeding R. Soc. London. 193 (1948) 281–297.